

Spatiotemporal analysis of human ovarian aging at single-cell resolution

Shixuan Wang

shixuanwang@t.jh.tjmu.edu.cn

Department of Obstetrics and Gynecology, Tongji Hospital, Tongji Medical College, Huazhong University of Science and Technology <https://orcid.org/0000-0002-8610-952X>

Meng Wu

Department of Obstetrics and Gynecology, Tongji Hospital, Tongji Medical College, Huazhong University of Science and Technology

Weicheng Tang

Department of Obstetrics and Gynecology, Tongji Hospital, Tongji Medical College, Huazhong University of Science and Technology

Ying Chen

Department of Obstetrics and Gynecology, Tongji Hospital, Tongji Medical College, Huazhong University of Science and Technology

Chuqing Wu

Department of Obstetrics and Gynecology, Tongji Hospital, Tongji Medical College, Huazhong University of Science and Technology

Xiaoran Zhu

Department of Obstetrics and Gynecology, Tongji Hospital, Tongji Medical College, Huazhong University of Science and Technology

Chaoyang Sun

Department of Obstetrics and Gynecology, Tongji Hospital, Tongji Medical College, Huazhong University of Science and Technology

Yan Li

Department of Obstetrics and Gynecology, Tongji Hospital, Tongji Medical College, Huazhong University of Science and Technology

Jinjin Zhang

Department of Obstetrics and Gynecology, Tongji Hospital, Tongji Medical College, Huazhong University of Science and Technology

Jun Dai

Department of Obstetrics and Gynecology, Tongji Hospital, Tongji Medical College, Huazhong University of Science and Technology

Su Zhou

Department of Obstetrics and Gynecology, Tongji Hospital, Tongji Medical College, Huazhong University of Science and Technology

Liru Xue

Huazhong University of Science and Technology

Dan Chen

Department of Obstetrics and Gynecology, Tongji Hospital, Tongji Medical College, Huazhong University of Science and Technology

Jiaqiang Xiong

Department of Obstetrics and Gynecology, Zhongnan Hospital, Wuhan University, Wuhan

Jing Yu

Shanghai Health Commission Key Lab of Artificial Intelligence (AI)-Based Management of Inflammation and Chronic Diseases, Sino-French Cooperative Central Lab, Shanghai Pudong Gongli Hospital, Second

Hongyi Li

College of Environmental and Resource Sciences, Zhejiang University, Hangzhou, Zhejiang

Yunfei Zhao

College of Food Science and Technology, Nanjing Agricultural University, Nanjing, Jiangsu

Yican Guo

Department of Obstetrics and Gynecology, Tongji Hospital, Tongji Medical College, Huazhong University of Science and Technology

Yibao Huang

Department of Obstetrics and Gynecology, Tongji Hospital, Tongji Medical College, Huazhong University of Science and Technology

Qingqing Zhu

Department of Obstetrics and Gynecology, Tongji Hospital, Tongji Medical College, Huazhong University of Science and Technology

Simin Wei

Department of Obstetrics and Gynecology, Tongji Hospital, Tongji Medical College, Huazhong University of Science and Technology

Junbao Gao

College of Plant Science and Technology, Huazhong Agricultural University, Wuhan, Hubei

Mingfu Wu

Department of Obstetrics and Gynecology, Tongji Hospital, Tongji Medical College, Huazhong University of Science and Technology

Ya Li

Department of Obstetrics and Gynecology, Tongji Hospital, Tongji Medical College, Huazhong University of Science and Technology

Tao Xiang

Department of Obstetrics and Gynecology, Tongji Hospital, Tongji Medical College, Huazhong University of Science and Technology

Article

Keywords: Human ovarian aging, spatiotemporal analysis, single-cell, cellular senescence, FOXP1

Posted Date: May 13th, 2022

DOI: <https://doi.org/10.21203/rs.3.rs-1624864/v1>

License:   This work is licensed under a Creative Commons Attribution 4.0 International License.

[Read Full License](#)

Additional Declarations: There is **NO** Competing Interest.

Version of Record: A version of this preprint was published at Nature Aging on April 9th, 2024. See the published version at <https://doi.org/10.1038/s43587-024-00607-1>.

Abstract

Our understanding of how aging affects the cellular and molecular components of the human ovary and contributes to age-related fertility decline is still limited. Here, we link single-cell RNA sequencing and spatial transcriptomics to characterize human ovarian aging. Changes of the molecular signatures of eight types of ovarian cells during aging were defined. We combined single cell types with their spatial location information to divide ovarian granulosa cells into three subtypes and theca & stroma cells into five subtypes. Further analysis revealed increased cellular senescence with age and characterized the transcription factor FOXP1 as a master regulatory gene during ovarian aging. Inhibition of FOXP1 in ovarian cells increased cellular senescence which was alleviated by pharmacological treatment with quercetin or fisetin. These findings provide a comprehensive understanding of the spatiotemporal variability of human ovarian aging, providing resources for developing new diagnostic biomarkers and therapeutic strategies against ovarian aging.

Introduction

Ovaries with the functions of fertility and hormone secretion play a vital role throughout the female reproductive lifespan¹. Ovarian function peaks at approximately 20 to 30 years of age, begins to decline after 30 years of age, and then reaches failure at approximately 50 years of age². Ovarian aging is a complex process governed by a gradual decrease in the quantity and quality of oocytes, with the final manifestation of sterilization and even menopause. Moreover, ovarian aging is considered the pacemaker of female body aging, which drives the aging of multiple organs³. After menopause, women will suffer from a number of organ dysfunctions for approximately 30 years, such as osteoporosis, cardiovascular disease, obesity, tumors, Alzheimer's disease and diabetes⁴. With the increase in life expectancy worldwide, ovarian aging has gradually become a key health problem among women. Therefore, an in-depth molecular understanding of human ovarian aging is of scientific and clinical importance.

The development of therapeutic strategies to delay ovarian aging requires accurate analyses of the cellular components and molecular properties of aged human ovaries. Human ovaries consist of different stages of follicles as basic functional units and a large number of stromal cellular elements⁵. Single-cell RNA sequencing (scRNA-seq), which is used to investigate cellular heterogeneity has facilitated the mapping of organ aging at unprecedented resolution⁶. Recent studies using scRNA-seq have indicated abundant cell types in human ovaries, such as granulosa cells, oocytes, stromal cells and immune cells^{7, 8}. However, the diverse cellular landscapes and cell type-specific regulatory changes during human ovarian aging are still unknown.

The human ovary shows extensive variation mainly in the cortex and medulla, with the processes of oogenesis starting in the cortex and the medullary region of the ovary undergoing dramatic restructuring. Thus, an understanding of spatial archetypes is necessary for a comprehensive understanding of the aging dynamics of the ovary. scRNA-seq technology requires the dissociation of tissue into a single-cell

suspension, increasing the difficulty of studying spatial architecture of the ovary. Although some in situ hybridization (ISH)-based methods have obtained spatial information, they only detect a few known target genes simultaneously^{9,10}. Spatial transcriptomics (ST) is a new technology that captures the mRNA of cells in sections using numerous barcoded oligo-dT primers and then maps transcripts to the tissue slice, enabling the spatial visualization of gene expression¹¹. This approach facilitates an analysis with subcellular resolution to confirm regional markers and cell type identities based on ST and scRNA-seq.

In this study, we aimed to explore the mechanism of human ovarian aging. We present a spatiotemporal atlas that systematically describes the spatial archetypes and cellular heterogeneity during the aging of the human ovary at three representative stages during ovarian cycles: optimal fertility (18–28 y), declining fertility (37–40 y) and the end of fertility (47–49 y). Then, utilizing spatial transcriptomics, we revealed the spatial position and dynamic variation of cells during ovarian aging and how they interacted with adjacent cells. In addition, we identified the contribution of cellular senescence to the development of aging-related ovary disorders and FOXP1 as a central protective factor for ovarian aging. Targeted inactivation of FOXP1 in human granulosa cells and theca & stroma cells aggravated cellular senescence, which was alleviated by pharmacological treatment with quercetin or fisetin. In conclusion, our data provide valuable inspiration for the mechanism and potential therapeutic targets of human ovarian aging.

Results

Single-Cell Transcriptome Profiling Identified Eight Cell Types in the Human Ovary

We obtained ovaries from women undergoing surgeries such as hysterectomy and oophorectomy because of cervical cancer or endometrial cancer. We chose three representative groups to better understand the mechanism of ovarian aging: young group (18y, 22y, 28y), middle group (37y, 38y, 39y), and old group (47y, 48y, 49y) (Table S1). The morphological analysis revealed more primordial follicles in the young group than in the middle and old groups, but more atretic follicles were observed in the older group (Figure S1A).

We applied 10x Genomics to the ovarian single-cell analysis to further investigate the mechanisms of human ovarian aging, especially the specific characteristics of each single cell. The 0.5–1cm³ ovary samples from women undergoing surgery were enzymatically dissociated into single cells within two hours (Fig. 1A), and the cell viability was greater than 80%. We obtained 92965 ovarian cells (31005 cells from young group, 32557 cells from middle group and 29403 cells from old group). Cells expressing high levels of mitochondrial genes (> 10% of total UMIs) were excluded (Figure S1B), and after quality control, only 63612 cells were retained for further analysis. The total cellular RNA content and number of expressed genes did not differ among the three groups (Figure S1C). Then, we used the UMAP algorithm

for the nonlinear dimensionality reduction analysis and identified eight cell types based on specific cell markers (Figs. 1B and S1D-S1F; Table S2). They were granulosa cells (GCs, *GSTA1*⁺, *AMH*⁺ and *HSD17B1*⁺), oocytes (OO, *TUBB8*⁺, *ZP3*⁺ and *FIGLA*⁺), theca & stroma cells (T&S, *DCN*⁺ and *STAR*⁺), smooth muscle cells (SMCs, *ACTA2*⁺ and *MUSTN1*⁺), endothelial cells (ECs, *TM4SF1*⁺ and *VWF*⁺), monocyte (MONO, *TYROBP*⁺ and *IFI30*⁺), Natural Killer cells (NK, *CCL5*⁺ and *NKG7*⁺), and T lymphocytes (T, *IL7R*⁺ and *KLRB1*⁺) (Figs. 1C and S1G). Similar to a previous study^{7,8}, T&S cells accounted for the majority of ovarian cells (Figure S1H). By comparing the cell types and the percentage of each type within the three groups, we found that the cell types and most cell densities did not differ with age. However, the percentage of smooth muscle cells increased and percentage of endothelial cells decreased (no significant difference) with age (Fig. 1D), which may be associated with vascular remodeling in the microenvironment of ovarian aging. Then we validated the specificity of markers of oocytes and granulosa cells (Figure S1I). In addition to classical markers such as *ZP3* for oocytes, we found that *TUBB8*, which encodes the primary beta-tubulin subunit expressed in oocytes¹², was also specifically distributed in oocytes. For granulosa cells, we found that *GSTA1* was specifically located in GCs, indicating that *GSTA1* may be a potential marker for granulosa cells. Furthermore, we performed a GO analysis of the marker genes of each cell type ensure the veracity of cell clustering (Fig. 1E). For example, the genes with high expression in GCs were enriched in the regulation of hormone levels, and those expressed at high levels in oocytes were enriched in oocyte differentiation. GO terms specific to T&S cells included “extracellular matrix organization” and “cholesterol transfer activity”. GO terms including “muscle system process” and “cytoskeleton organization” were enriched in SMCs. Collectively, our data represent the first single-cell transcriptomic map for human ovarian aging, which illuminated the cell composition of the human ovary and the changes with age.

Spatial Location of Human Ovarian Cells

We performed ST on tissues collected from across ovarian aging (3 sections from 3 samples; young, n = 1; middle, n = 1; old, n = 1) to map spatial distributions of the cells identified using scRNA-seq data. In the human ovarian ST-seq data, the mtRNA of all ST spots represented less than 20% of the total reads, indicating good data quality (Figure S2A). Then, SCTransform was used to normalize the data (Figure S2B). ST-seq of the human ovary collectively detected over 21,000 genes (Figures S2C and S2D), and the location of follicles was detected with higher UMIs and more genes (Figure S2C).

Using the scRNA-seq atlas, we performed a factor analysis to determine the likely single-cell composition of each spot, thus spatially localizing all scRNA-seq clusters. These well-characterized cell types were localized, such as oocytes in the middle of the follicle (Fig. 2A), granulosa cells in the outer follicle (Fig. 2A), theca & stroma cells (Fig. 2A) that were widely distributed, and smooth muscle cells/endothelial cells that were distributed toward the blood vessel (Figs. 2A and 2A). The immune cells, including monocytes, Natural Killer cells and T lymphocytes, were mainly distributed in the interstitium of the medulla, atretic follicles and corpus luteum (Figs. 2A , 2A and 2A). The overall distribution of all cells is shown in Figure S2E. Furthermore, after modeling the spatially resolved

expression of marker genes for different types of cells, we observed that the local expression of the oocyte marker genes *ZP3* and *TUBB8* predicted the location of oocytes (Fig. 2A), the granulosa cells marker genes *AMH* and *GSTA1* predicted the location of granulosa cells (Fig. 2A), the theca & stroma cells marker genes *DCN* and *STAR* predicted the location of theca & stroma cells (Fig. 2A), *ACTA2* and *MUSTN1* predicted the location of smooth muscle cells (Fig. 2A), *TM4SF1* and *VWF* predicted the location of endothelial cells (Fig. 2A), *TYROBP* and *IFI30* predicted the location of monocyte (Fig. 2A), *NKG7* predicted the location of Natural Killer cells (Fig. 2A), *IL7R* predicted the location of T lymphocytes (Fig. 2A).

The human ovarian structure includes the cortex, transition region and medulla. We wanted to determine whether the transcriptional/cellular spatial variability corresponds to the tissue depth. We identified 142 depth-associated genes, reflecting pathways active in different layers: (Fig. 2B)—the surface region enriched for the response to temperature stimulus, regulation of response to stimulus and response to incorrect protein progressing toward response and stimulation to the outside, indicating that the ovarian surface is vulnerable to internal and external stimulation; and, deeper spots enriched for translational initiation, RNA catabolic process, and cotranslational protein targeting to membrane progressing toward gene expression, indicating that there is an active biological process in the deeper part of the ovaries.

Gene Expression in Different Cell Types Changed Throughout Human Ovarian Aging

We compared the gene expression patterns of ovarian cell types between the young, middle and old groups to further explore the mechanism of ovarian aging at the cellular level. We identified thousands of differentially expressed genes (DEGs, $|\text{avg_logFC}| > 0.25$ and $p\text{-val_adj} < 0.05$) in at least one cell type of the human ovary during aging (Figs. 3A and 3B; Table S4). A total of 1068, 711, and 889 upregulated DEGs were identified between the young and old (O/Y) groups, young and middle-aged (M/Y) groups, and middle-aged and old (O/M) groups, respectively (Fig. 3C). In comparison, 1187, 376, and 1241 downregulated DEGs were identified in the O/Y groups, M/Y groups, and O/M groups, respectively (Fig. 3C). Among all ovarian cell types, oocytes showed the greatest difference among the three groups (Figure S3A). Notably, the analysis of DEGs revealed a substantial difference between the perimenopausal ovaries and the young or middle-aged ovaries with reproductive function.

We aligned datasets from individual samples by their chronological age and clustered the DEGs by their expression patterns to identify the constantly upregulated or downregulated DEGs during aging. Using this method, we identified 5,476 age-dependent upregulated DEGs and 3,412 age-dependent downregulated DEGs in eight cell types (Fig. 3D; Table S5). GO and KEGG enrichment analyses revealed that age-related upregulated genes were mainly associated with cellular senescence, the FoxO signaling pathway, the IL-17 signaling pathway, the nuclear factor- κ B (NF- κ B) signaling pathway, the NOD-like receptor signaling pathway, the p53 signaling pathway, the PI3K-Akt signaling pathway and the transcriptional misregulation in cancer (Fig. 3E). Age-related downregulated genes were mainly related to cell migration, ECM-receptor interaction, estrogen signaling pathway, extracellular vesicle, oxidative

phosphorylation, platelet activation, regulation of actin cytoskeleton and tight junction (Fig. 3E). Similarly, a pathway analysis of the spatial gene expression data indicated increased enrichment of cellular senescence and the p53 signaling pathway, while we identified decreased enrichment of estrogen signaling pathway and oxidation phosphorylation within the old ovary (Fig. 3F).

Based on the aforementioned results, cellular senescence, a process that results from a variety of stresses and leads to a state of irreversible growth arrest, may play an important role in human ovarian aging. We compared the core senescence gene list from the GeneAge database to our scRNA-seq data and generated a cellular senescence score to assess the senescent cell fraction¹³. The cellular senescence score was significantly increased in multiple cell types during ovarian aging (Figs. 3G and S3B). We further detected lipofuscin, which accumulates mainly in aged cells and is considered a hallmark of cellular senescence¹⁴, in human ovaries from patients of different ages. As shown in Fig. 3H, lipofuscin accumulation was increased in aged ovarian tissues. The expression of CDKN1A/p21, the core senescence marker, was significantly increased in ovarian cells from the old group compared to the young or middle group (Figure S3C). Additionally, we identified the spatial expression of CDKN1A in the three groups using spatial transcriptomic data, and showed increased activity in the ovarian cortical region during aging (Figure S3D). We further validated the finding by performing immunostaining and found that increased numbers of CDKN1A-positive cells accumulated during ovarian aging (Fig. 3I). Consistently, we also observed increased CDKN1A mRNA expression in aged ovaries (Figure S3E), indicating that increased numbers of senescent cells may underlie ovarian aging. Furthermore, cellular senescence is also accompanied by chronic inflammation. We observed that inflammatory response genes and the NF- κ B signaling pathway, which in turn induce the senescence-associated secretory phenotype (SASP) and aggravate cellular senescence¹⁵, were activated in most cell types during ovarian aging (Figures S3F and S3G). Collectively, these results indicate that a series of molecular changes, especially cellular senescence and the inflammatory response, occur in aged human ovaries and likely contribute to the development of aging-related ovarian disorders.

Changes in Oocytes during Human Ovarian Aging

We next sought to identify aging-associated changes in gene expression in oocytes. We performed a pseudotime trajectory analysis to analyze the origin and maturation of oocytes (Fig. 4A). All oocytes in the young group were identified as Stage_a and Stage_b cells, most oocytes in the middle group were identified as Stage_a and all oocytes in the old group were predominantly classified in Stage_c cells (Fig. 4B). This pseudotime analysis showed that the oocyte in young group were at the beginning of the trajectory path, whereas the oocytes in old group were at a terminal state, which showed that the oocytes undergo GeneSwitch in the process of aging (Fig. 4C). Next, we further analyzed the dynamic changes in the gene expression pattern at each stage. A total of 356, 219, and 3 DEGs ($p_{adj_val} < 0.05$, $\log_2FC > 0.5$) were observed in the three states, respectively (Fig. 4D). Then, we performed a GO analysis of DEGs at each stage. In Stage_a cells, the main enriched GO terms were “cotranslational protein targeting to membrane,” “nuclear-transcribed mRNA catabolic process,” and “translational initiation” (Fig. 4E), suggesting that oocytes at this stage exhibit active biological processes. In Stage_b cells, “collagen-

containing extracellular matrix”, “extracellular matrix organization”, and “positive regulation of cell adhesion” were enriched (Fig. 4E). In Stage_c cells, the main enriched GO terms were “organelle fission”, “polysomal ribosome” and “double-strand break repair” (Fig. 4E), indicating that oocytes in Stage_c undergo DNA damage and cell stress (Fig. 4E). A recent study revealed that the DNA damage response (DDR) is the primary biological pathway that regulates reproductive senescence¹⁶. We compared the DNA damage and repair gene list and generated DNA damage and repair scores. With aging, DNA damage genes were upregulated in oocytes (Fig. 4F). The expression of classical DNA damage response genes, such as STAT3 and EIF4A1, was markedly upregulated in old oocytes (Fig. 4F). However, DNA repair genes that are crucial for the maintenance of oocyte homeostasis, such as APEX1 and RAD1, were downregulated in old oocytes (Fig. 4G). Consistently, we observed the accumulation of DNA oxidation (8-OHdG-positive cells), DNA damage (γ H2AX-positive cells), and protein oxidation (nitrotyrosine-positive cells) in aged oocytes (Figs. 4H and 4I).

Changes in the Transcriptional Profiles of the Three Subpopulations of Granulosa Cells during Human Ovarian Aging

Granulosa cells of the ovarian follicle surround and interact with the developing oocyte, and are responsible for estrogen and progesterone synthesis. First, we explored the heterogeneity of human granulosa cells. UMAP analysis classified all the granulosa cells into three groups (granulosa cell subtypes 1–3) (Fig. 5A; Table S2). Statistics indicate that granulosa cells in the young group were mainly granulosa cell subtype 1 and 2, and the granulosa cells in the old group were mainly granulosa cell subtype 3 (Fig. 5B). Further analysis of the expression levels of the markers showed granulosa cell subtype 1 was characterized by the expression of the known markers AMH, FST, HSD17B1, SERPINE2, and PRKAR2B, as well as several genes that had not previously been associated with granulosa cells, such as TNNI3, DSP, and MAGED2 (Fig. 5C). The GO analysis revealed the biological processes that were enriched for follicular development. Notably, “ATP metabolic process” and “Gap junction” were enriched in granulosa cell subtype 1 (Fig. 5D). Granulosa cell subtype 2 was characterized by the expression of genes related to hormone synthesis, such as INSL3, APOE, GSTA1, APOA1, FDX1 and CYP17A1 (Fig. 5C). Similarly, GO terms, including “cholesterol metabolic process” and “steroid biosynthetic process” were enriched in granulosa cell subtype 2 (Fig. 5D). In addition, granulosa cell subtype 3 by the expression of the markers DCN, LGALS1 and LGALS1, which were reported to regulate the apoptosis and cell cycle of granulosa cells^{17,18} (Fig. 5C). Notably, “Apoptosis” and “Cell cycle” were enriched in granulosa cell subtype 3 (Fig. 5D).

Since each individual spot on the spatial transcriptomic slide putatively contains multiple cells, we transferred the labels from the integrated data to spatial gene expression data and mapped different cell types based on spatial location (Fig. 5E). Interestingly, we observed three different populations of granulosa cells in three distinct areas. Granulosa cell subtype 1 was located in the cumulus of the antral follicle, granulosa cell subtype 2 was located in mural layer of follicles, while granulosa cell subtype 3 showed a broad distribution across antral follicles and the ovarian cortex (Fig. 5E).

We next explored the dynamic states and cell transitions in granulosa cells by inferring the state trajectories using Monocle. This analysis showed that granulosa cell subtype 1 was at the beginning of the trajectory path (Figs. 5F and 5G). We analyzed the trajectories of granulosa cells in the three groups separately to further delineate the transition states associated with granulosa cells in different samples. Surprisingly, early-stage granulosa cell subtype 1 was predominantly distributed in young samples, whereas granulosa cells in old samples were primarily at the terminal ends of the granulosa cell subtype 3, indicating that the granulosa cells undergo GeneSwitch during the ovarian aging (Fig. 5H). We next investigated the transcriptional changes associated with transitional states and observed that the granulosa cell clusters were categorized into 3 phases (Fig. 5I). Granulosa cell subtype 1 was predominantly phase 1 cells, and pathway analysis indicated that signaling pathways involved in the metabolism of GTP and glucose. This finding indicated that phase 1 cells were more closely related to metabolism and that these metabolites may reach the oocyte via paracrine signals and gap junctions to promote follicular development. Pathway analysis suggested that cells in phase 2 were enriched in the apoptosis pathway, matching the characteristics of granulosa cell subtype 3. Phase 3 was characterized by genes involved in cytokine production and extracellular matrix, further confirming the hormone synthesis function of granulosa cell subtype 2. Collectively, the above results indicated that granulosa cells can be divided into three subtypes, with granulosa cell subtypes 1 and 2 have better function, mainly in the young and middle ovaries, while granulosa cell subtype 3 was mainly present in the old ovaries.

As apoptosis of granulosa cells causes follicular atresia and ovarian aging (Matsuda et al., 2012), we next focused on the aging-associated changes in gene expression in granulosa cells. Further dissection of the transcriptomic changes in these subpopulations during aging showed that DEGs in granulosa cells between the young, middle and old groups partially overlapped among different subpopulations (Figures S4A and S4B). We also identified age-related DEGs in each subpopulation by performing a hierarchical clustering analysis (Figure S4C; Table S5). We calculated the cellular senescence score to determine whether cell senescence are also changed in granulosa cells during aging, and the results showed that it was augmented in all types of granulosa cells in the aged ovary (Fig. 5J). Accordingly, CDKN1A, a molecular marker of senescent cells, was upregulated in three subpopulations of granulosa cells (Figs. 5K and S4D). We obtained human granulosa cells (hGCs) from healthy women aged 21 to 46 years old to further validate the senescence of granulosa cells (Figures S4E). We also observed aging-associated increases in the expression CDKN1A, CDKN2A and SASP (IL-6 and IL-8) in hGCs from healthy donors, further supporting cellular senescence in hGCs during physiological aging. Finally, we performed a transcriptional regulatory network analysis for each granulosa cell subpopulation and identified preferential transcriptional regulons in each subpopulation (Fig. 5L). FOS, SOX4, FOXP1 and KLF2 served as core downregulated transcription factor (TF), while JUND, CEBPD, FOSB and IRF1 served as core upregulated transcription factor at the hub of transcriptional regulatory networks of granulosa cells in different subpopulations during aging (Figs. 5L and S4F). Altogether, these findings suggest that cellular senescence is a feature of aging granulosa cells, likely contributing to ovarian dysfunction during aging.

Changes in the Transcriptional Profiles of the Five Subpopulations of Theca & Stroma Cells during Human Ovarian Aging

The ovary contains a large stromal compartment, including the tunica albuginea, interstitial stromal and theca interna¹⁹. However, the classification of ovarian stromal cells and whether stromal cell subpopulations respond differently to aging are not clear. Using unbiased clustering and UMAP analyses, we identified five types of theca & stroma cells with distinct cellular transcriptomic signatures (Fig. 6A; Table S2). Furthermore, we analyzed the changes in the gene expression pattern in each subpopulation of theca & stroma cells. An analysis of the expression levels of the markers showed that theca & stroma cells subtype 1 was characterized by the expression of the markers *STAR* and *CYB5A* (Fig. 6B). The GO analysis revealed that the biological processes RNA and protein synthesis were enriched in theca & stroma cell subtype 1 (Fig. 6C). Theca & stroma cell subtype 2 was characterized by the expression of genes associated with the extracellular matrix, such as *COL1A1*, *COL3A1* and *COL1A2* (Fig. 6B). Accordingly, the GO analysis revealed that “Extracellular vesicle” and “Extracellular matrix” were enriched in theca & stroma cell subtype 2 (Fig. 6C), consistent with their function in maintaining the morphology and function of follicles. Theca & stroma cell subtype 3 expressed markers of myofibroblast-like fibroblast states, as evidenced by the increased expression of *ACTA2* and *TAGLN* (Fig. 6B). These cells were further enriched for pathways related to supramolecular fiber, muscle system process and cytoskeletal protein binding (Fig. 6C). Theca & stroma cell subtype 4 was defined by *FBLN1* and *CXCL2* expression (Fig. 6B). Consistent with gene expression patterns, the GO analysis revealed an enrichment of “response to chemical” and “regulation of response to stimulus” (Fig. 6C). Theca & stroma subtype cell 5 had features of inflammatory-like fibroblasts, with high expression of markers (*CD74*, *HLA-DRB1*, *CCL4* and *HLA-DRA*) and pathways related to “antigen processing and presentation” and “cellular response to interferon-gamma and complement cascades” (Figs. 6B and 6C). Statistics indicate decreased numbers of theca & stroma cell subtype 2 and theca & stroma cell subtype 5 in the old group, consistent with the decrease in the number of follicles in the old ovary (Figure S5A).

We spatially located five subpopulations of theca & stroma cells to integrate the scRNA-seq and ST data (Fig. 6D). Interestingly, we observed the theca & stroma cell subtype 1 was widely distributed in the ovarian medulla. Theca & stroma cell subtype 2 was distributed around the follicle, and may be involved in the development of follicles. Theca & stromal cell subtype 3 was located around the blood vessels, and the GO analysis showed that these cells are probably a group of stroma cells that maintain vasoconstriction. Theca & stroma subtype cell 4 was distributed in the outer cortex, consistent with the GO analysis, and play roles in ovarian defenses against external stress. Theca & stroma cell subtype 5 was distributed in the repair area after ovulation, consistent with their immunoregulatory properties, suggesting that they are involved in the inflammatory response and ovarian repair after ovulation. Taken together, the results highlighted that the spatiotemporal dynamic landscape of theca & stromal cells subpopulations were closely related to their function.

Furthermore, we selected the regions of different follicle stages for comparison to obtain insights into the spatial organization of theca & stroma cell types. According to H&E staining of the ovary section, region 1 represents healthy follicle, and the regions 2 and 3 represent atretic follicles. Region 4 is the disappearing corpus luteum after ovulation with many monocytes and endothelial cells. In region 5, theca & stroma

cells have replaced the corpus luteum (Figure S5B). The distribution of different types of theca & stroma cells was associated with their appropriate function (Figure S5C), and they showed distinct gene expression patterns (Figure S5D). By comparing the transcriptome datasets of healthy follicle (region 1) with that of the atretic follicle (region 2), we observed that the process of “ferroptosis, lysosome, autophagy, apoptosis and necroptosis” was enriched in region 2 (Figure S5E), suggesting that multiple cell death patterns are involved in the regulation of follicular atresia. We also analyzed the changes of the absorption process of the corpus luteum (region 4 and region 5), the data demonstrated theca & stroma cells in region 4 were enriched in the process of “ferritin complex, sequestering of iron ion, ferric iron binding, ferroptosis and mineral absorption” (Figure S5E), highlighting that iron metabolism plays an important role in the absorption of the corpus luteum.

T-SNE analysis helped to reveal heterogeneity among theca & stroma cells, and we also wondered if they shared common differentiation trajectories. Theca & stroma cells from different subclusters were distributed broadly across the pseudotime space, with theca & stroma cell subtype 2 primarily occupying the beginning of the trajectory path, whereas the remaining half mainly consisted of theca & stroma cell subtype 1 (Fig. 6E). We analyzed the trajectories of theca & stroma cells in young, middle and old groups separately to further delineate the transition states associated with theca & stromal cells in samples from patients of different ages. Surprisingly, early-stage theca & stroma cells were predominantly distributed in young and middle samples, with few cells identified at the end of the cell state transition path, whereas theca & stroma cells in old samples were primarily located at the terminal ends of the transition path (Fig. 6F). We next investigated the transcriptional changes associated with transitional states and observed that the theca & stromal cell clusters were categorized into 3 phases (Fig. 6G). Theca & stroma cell subtype 2 was predominantly phase 1 cells involved in the metabolic process and extracellular matrix, suggesting that these cells play an important role in follicle development. The other types of theca & stroma cells were all distributed in phase 2 and phase 3, suggesting limit changes in differentiation trajectories.

Furthermore, we analyzed age-dependent alterations in gene expression in the theca & stroma cells represented in our dataset. Dissection of the transcriptomic changes in these subpopulations during aging showed that DEGs in theca & stroma cells between the three groups largely overlapped among different subpopulations (Figure S5F). We also identified age-related DEGs in each subpopulation by performing a hierarchical clustering analysis (Figure S5G; Table S5), which again showed that many of them were shared across subpopulations. In addition, we observed higher cell senescence scores in all subpopulations of theca & stroma cells during aging (Fig. 6H). Accordingly, CDKN1A was upregulated in aged theca & stroma cells, which may be a consequence of ongoing cellular senescence (Figs. 6I and S5H). Finally, we performed a transcriptional regulatory network analysis for each theca & stroma cells subpopulation and identified preferential transcriptional regulons in each subpopulation (Fig. 6J). MYC, CEBPD, CREM and IRF1 were activated in a cell type-specific manner during ovarian aging, serving as core upregulated transcription factor. FOXP1, FOS, SOX4, ARX and JUN (Figure S5I), which showed decreased expression in aged theca & stroma cells, served as core downregulated transcription factor.

FOXP1 Exerted Geroprotective Effects on Human Ovarian Aging

Based on the results described above, cellular senescence may be involved in the regulation of ovarian aging. The transcription factor analysis of granulosa cells and theca & stroma cells indicated that FOXP1, SOX4 and FOS, which regulate the cellular senescence of both granulosa cells and theca & stroma cells, may be the core TFs involved in ovarian aging. We knocked down FOXP1, SOX4 and FOS using siRNAs in a human granulosa cell line (COV434) and primary theca & stroma cells (pT&S) to determine the roles of FOXP1, SOX4 and FOS in ovarian aging. Inspiringly, si-FOXP1 and si-SOX4 transfection in COV434 and pT&S cells resulted in a stable increase in the expression of cell senescence-associated genes, including CDKN1A and CDKN2A, but not si-FOS group (Figure S6A). We further examined the expression of FOXP1 and SOX4 in human ovaries and observed decreased expression of both with age (Figs. 7A and 7B). Similarly, we observed aging-associated increases in FOXP1 and SOX4 expression in hGCs from healthy donors (Fig. 7C). We speculate that the transcription factor FOXP1 and SOX4 may affect ovarian function by regulating cell senescence. Then, we silenced FOXP1 or SOX4 expression by using small interfering RNAs (siRNAs) in COV434 and pT&S cells. SA- β -gal staining showed that FOXP1 knockdown promoted the senescence of COV434 and pT&S cells, and si-SOX4 only lead to the senescence of COV434 cells (Figs. 7D and S6B). In addition, the protein expression of cellular senescence-, inflammation- and DNA damage-related genes increased upon knockdown of FOXP1 and SOX4 in COV434 or pT&S cells (Figs. 7E and S6C). Moreover, FOXP1 and SOX4 knockdown decreased the percentages of EdU-positive and Ki67-positive cells (Figs. 7F and S6D-6G), indicating that the downregulation of FOXP1 and SOX4 in human ovarian granulosa cells and theca & stroma cells led to decreased proliferation. The activation of the DNA damage response is one of the main mediators of cell senescence, which results in irreversible growth arrest²⁰. We also observed an increased fluorescence intensity of γ H2AX in COV434 and pT&S cells upon knockdown of FOXP1 and SOX4 (Figures S6D, S6E and S6H). Together, these data indicate that an age-related decrease in FOXP1 and SOX4, especially FOXP1, which regulates the senescence of both granulosa cells and theca & stroma cells, may be an important contributor to ovarian aging.

We further explored the molecular mechanism underlying the age-related downregulation of FOXP1 and its role in human ovarian aging. Genome-wide RNA-seq analysis further revealed that FOXP1 knockdown in COV434 cells upregulated 118 genes and downregulated 405 genes (Figures S6I-S6K). The GO analysis showed that the upregulated genes were enriched in the terms “response to stimulus” and “immune response” upon knockdown of FOXP1, whereas the downregulated genes were mainly associated with “cellular developmental process” and “cell differentiation” (Fig. 7G). At the same time, the expression of senescence markers (CDKN1A, CDKN2A, and CDKN2B) the SASP (IL6, TNF, and CXCL8) was significantly higher in the si-FOXP1 groups than in the controls (Fig. 7H). Moreover, si-FOXP1 resulted in an increase in the expression of molecules in the NF- κ B, TNF, NOD-like receptor, p53 and DNA damage pathways, which are both associated with cell senescence and immune inflammation (Figure S6L). We next asked whether these transcriptional changes in the human granulosa cell line were similar to those in human GCs during ovarian aging. Fifteen genes were upregulated both in FOXP1-knockdown COV434

cells and GCs from aged human ovaries, including IFITM1, IL1R1, ISG20, CFH, SOD2, CXCL2 and ISG15, which are involved in immune inflammation homeostasis (Figure S6M). In addition, ChIP-PCR was performed using the FOXP1 antibody in COV434 cells to verify whether FOXP1 directly bind to the CDKN1A promoter (Fig. 7I). These findings suggested that FOXP1 restrains ovarian cell senescence by repressing CDKN1A transcription during ovarian aging.

We subsequently explored whether three well-studied senolytics (fisetin, quercetin and dasatinib) fighting cell senescence reversed ovarian aging²¹. Encouragingly, we observed that quercetin and fisetin delayed cellular senescence induced by FOXP1 knockdown (Figs. 7J and 7K). Accordingly, we observed reduced levels of senescence and inflammatory markers in fisetin- or quercetin-treated COV434 cells (Fig. 7L). In addition, fisetin and quercetin improved the proliferation rate of COV434 cells (Figs. 7M and S7A). Immunofluorescence staining also showed reduced levels of the DNA damage response marker γ -H2AX after treatment with fisetin or quercetin (Figure S7B). On the other hand, quercetin significantly decreased the levels of the CDKN1A and CDKN2A mRNAs, and both fisetin and quercetin decreased the secretion of senescence-associated cytokines (Figure S7C). These findings suggested that senolytics may prevent ovarian cells from senescence and are promising senolytics for ovarian aging, especially quercetin.

Vascular Remodeling during Human Ovarian Aging

The ovarian vasculature is important for follicle activation, growth, survival and the generation of a corpus luteum capable of maintaining pregnancy²², while little is known about the changes in blood vessels during human ovarian aging. Morphologically, senile blood vessels exhibited characteristics of vascular aging, including increased wall thickness, increased fibrosis and lipid accumulation of the tube wall, determined by histological analysis, Masson's staining, Sirius red staining and Oil red staining (Figs. 8A and S8A). As verified by immunofluorescence staining, we observed that CD31, a marker of ECs, labeled a curly shape in aged ovaries (Fig. 8B). Furthermore, the expression of α -SMA, a characteristic marker of SMCs, was upregulated in the vessels of aged ovaries (Fig. 8B). Together, the age-dependent structural changes in the vascular system in the human ovary include the endothelium and vascular smooth muscle cells.

We further explored age-associated ovarian vascular transcriptomics at single-cell resolution. The cells from vessels were grouped into five clusters, including endothelial cells (arterial ECs, venous ECs and capillary ECs) and smooth muscle cells (arterial SMCs and venous SMCs) (Fig. 8C). ECs were present at a higher percentage in the young group than in the middle or old group, whereas the percentages of arterial SMCs in the old group were higher than those in the young or middle group (Figure S8B). Next, scRNA-seq and ST datasets were integrated to characterize the locations of ECs and SMCs. We observed that the distribution of ECs and SMCs overlapped with the location of blood vessels (Figure S8C), further confirming the accuracy of cell clustering.

Annotations were guided by the expression of canonical cell class markers, as exemplified in Figs. 8D and S8D. Consistent with the function of these marker genes, GO and KEGG analysis revealed unique transcriptional features and enriched pathways relevant to their distinct physical functions (Figs. 8E, S8E

and S8F). For example, arterial ECs were primarily associated with the KEGG term “intercellular communication”. Notably, venous ECs exhibited a predominance of vascular remodeling pathways. In addition, “extracellular matrix” and “blood vessel morphogenesis” were enriched in capillary ECs. We next investigated the gene expression patterns in SMCs, and the results showed that muscle contraction and extracellular matrix were enriched in arterial SMCs and venous SMCs, respectively (Figs. 8E and S8F).

We next compared the single-cell transcriptomes of ECs and SMCs during ovarian aging. We compared cell-intrinsic gene expression programs of the same cell types between the three groups and identified 778 upregulated and 522 downregulated genes (\log_2 [fold change] ≥ 0.5 and adjusted p value ≤ 0.05 , referred to as young/middle/old differentially expressed genes), that were differentially expressed in at least one type of vascular cell (Fig. 8F). The core pathways annotated for upregulated DEGs that were shared by diverse vascular cell types involved inflammation and aging pathways, such as response to stress, immune response, cell death and cell senescence (Fig. 8G). In comparison, annotated pathways for downregulated DEGs that were shared by disparate vascular cell types included vasculature development, angiogenesis, extracellular matrix and estrogen signaling pathway (Fig. 8G). These observations were consistent with vessel abnormalities that we observed in aged human ovarian arteries.

According to the results shown in Fig. 3, ECs and SMCs from human ovarian tissue exhibit characteristic transcriptomic features of cellular senescence during aging. Cellular senescence may result in proatherosclerotic, proinflammatory, and prothrombotic changes in vascular function and contribute to the age-related vascular disease. Furthermore, we evaluated whether the senescence of ECs and SMCs drives vascular aging. The expression of the core senescence marker CDKN1A was significantly increased in all subtypes of ECs and SMCs (Fig. 8H). Similarly, we observed increased levels of the CDKN1A protein during ovarian aging (Fig. 8I). Moreover, the level of SASP score was significantly increased in ECs and SMCs, indicative of the cellular senescence state in the aged ovary (Fig. 8J). Furthermore, the cellular senescence associated pathway, NOD-like receptor signaling pathway and TNF signaling pathway were increased in ECs and SMCs during ovarian aging (Figure S8G). Similarly, the TF FOXP1 was decreased in the SMCs of middle and old group compared with that of young group (Figure S8H). Cellular senescence promote age-related extracellular matrix remodeling²³. SMCs are the major source of ECM, especially collagens and proteoglycans. Noticeably, the expression of Timp1, a major contributor to vascular remodel, was increased in both arterial and venous MSCs (Figure S8I). Altogether, ECM-senescent cells interactions might contribute to vascular remodel in aged human ovaries.

Discussion

In this study, we analyzed single-cell and spatial transcriptomic maps of human ovaries from young, middle, and old-aged individuals to comprehensively characterize spatial and temporal differences in gene expression during ovarian aging. Based on this dataset, our analyses provided five noteworthy contributions. First, we elucidated gene expression signatures for eight types of human ovarian cells, identified thousands of cell type-specific DEGs during human ovarian aging, and charted the nature of their crosstalk with neighboring cells. Second, an analysis of age-associated changes in gene-expression

revealed that the DNA damage response is the primary biological pathway that regulates oocyte senescence. Third, the scRNA-seq data combined with ST data facilitated the identification of three granulosa cells subtypes and four theca & stromal cells subtypes in the human ovary, as well as the changes in transcriptomic features during aging. Fourth, we drew a map of the transcriptional changes that occur in vascular cells and revealed vascular remodeling during human ovarian aging. Fifth, the data revealed that cellular senescence may trigger ovarian aging and identified FOXP1 as a central protective factor to eliminate accumulated senescent cells and to restore tissue function. Altogether, these observations provide novel insights into human ovarian aging and identify new biomarkers and targets for the diagnosis and treatment of ovarian aging.

Because of the difficulty in obtaining critical human tissues, few studies have assessed the cellular compositions and gene expression in adult and aged ovaries. Wang et al. recently used the scRNA-seq technique to generate a nonhuman primate cell atlas for ovarian aging²⁴. Although nonhuman primates are recognized as the best animal model for human studies, many evolutionary differences exist between nonhuman primates and humans^{25,26}. Llonch et al. characterized and compared the transcriptomes of germinal vesicle stage (GV) and in vitro-matured (MII) oocytes from women of varying reproductive ages²⁷. However, their study was restricted to oocytes after ovulation, not developing oocytes and ovarian somatic cells. In this study, we present the first comparative atlas of temporal and spatial variability in old versus young human ovarian tissues, providing data to uncover in-depth age-related alterations in gene expression in oocytes and ovarian somatic cells at the single-cell level.

We show that oocyte senescence is related to a compromised DDR. Somatic cell aging is associated with age-induced accumulation of DNA double-strand breaks (DSBs) and the inability to repair this damage appropriately^{28,29}. Based on this concept, researchers have hypothesized that DNA damage and a loss of DNA repair capacity contribute to oocyte aging. In humans, primordial follicles may be quiescent for several decades, highlighting the importance of potential DNA damage accumulation that may threaten genomic integrity, cellular function and viability^{30,31}. A microarray analysis of young and old metaphase II oocytes showed significant changes in the expression of genes related to DNA stability and DNA repair³². Other studies have shown that DNA damage in oocytes may result in dysfunctional meiosis and germ cell apoptosis^{33,34,35}. By performing a scRNA-seq analysis, we showed the activation of the DNA damage system in aged oocytes and a decrease in their capacity to repair damaged DNA, as evidenced by the levels of DNA oxidation and damage markers in aged oocytes. However, due to the limitation of sequencing technology, we were only able to detect oocytes with a diameter of less than 50 μm , including oocytes of primordial follicles and partial primary follicles³⁶. Therefore, spatiotemporal transcriptomic analysis of other ovarian oocyte stages might be needed in future studies.

As a feature of aging, cellular senescence is a stress response designed to inhibit the proliferation of aged or damaged cells, ultimately leading to a state of permanent growth arrest in which cells secrete a range of proinflammatory and proteolytic factors as part of the SASP³⁷. However, researchers have not determined whether the accumulation of senescent cells leads to ovarian aging. Through a

spatiotemporal transcriptomic analysis, our findings show that most cell types in aged ovaries show virtually all established features of cellular senescence. These changes include increased cellular senescence score, SASP, SA- β -gal activity, lipofuscin accumulation, increased oxidative protein damage, and changes in the expression of molecules involved in cellular senescence pathways. Previous studies indicated that two pathways can initiate and maintain cellular senescence: the p53-p21-pRB and the p16-pRB pathways³⁸. Here, we describe a significant increase in CDKN1A/p21 levels in eight ovarian cell types, suggesting that a p21 pathway-induced senescence-like phenotype may be present in aged human ovaries. Histological assessments and transcriptional analyses of mouse ovaries revealed significantly increased CDKN1A expression with advancing age³⁹. In line with this finding, endometriosis induced ovarian aging can lead to the increase of CDKN1A⁴⁰. These findings further link ovarian cell senescence to the p21 pathway. The prolonged presence of senescent cells in the tissue is problematic because the SASP secretes proinflammatory factors that trigger local inflammation and spread the senescence phenotype⁴¹. Our results reveal that the senescent cells in the ovary have the characteristics of secreting SASP factors, inducing the activation of the NF- κ B pathway and inflammatory response genes, which further reinforce senescence.

The molecular network orchestrating the balance between the proliferation and senescence of ovarian cells remains largely unknown. In this study, our analyses identified FOXP1 as a key transcription factor regulating cellular senescence in the human ovary. Here, we show decreased expression of FOXP1 in ovarian granulosa cells and stromal cells. We also observed that FOXP1 deficiency resulted in prototypical premature aging of granulosa cells or theca & stroma cells. FOXP1 is a transcription factor that controls the cell differentiation, proliferation and development^{42, 43, 44}. A recent study further revealed an important role for FOXP1 in mesenchymal stem cell senescence⁴⁵. The role of FOXP1 in the ovary has rarely been reported, and only one study revealed that miR-1181 might promote ovarian tumorigenesis by downregulating FOXP1⁴⁶. A central finding of our study is that FOXP1 attenuates human ovarian cell aging by directly regulating CDKN1A transcription, linking FOXP1 to cellular senescence (Fig. 9). However, further studies such as ChIP-sequencing could be conducted to obtain a deeper understanding of the global transcriptional regulatory network of FOXP1 in ovarian cellular senescence.

Vascular remodeling is another feature of human ovarian aging we identified. A multitude of biological processes contribute to vascular remodeling, such as inflammation, oxidative stress, lipid accumulation, and degradation of the ECM⁴⁷. During ovarian aging, we found that ECs and SMCs become senescent and acquire an SASP, characterized by increased secretion of proinflammatory mediators. We propose that senescent cells and their SASPs contribute to vascular remodeling in aged ovaries. EC senescence is an essential step for the initiation of vascular aging and contributes to the development and progression of age-related cardiovascular diseases⁴⁸. Binet et al. verified that the elimination of senescent vascular cells ameliorates neovascular retinal disease⁴⁹. These findings indicate that cellular senescence is an essential step in the development of vascular aging. In addition, the role of vascular remodeling in the ovarian aging process has also recently received attention⁵⁰. This function is supported by the finding

that the size of atherosclerotic plaque was negatively correlated with ovarian reserve in female monkeys⁵¹. Moreover, women with a history of preeclampsia, a condition characterized by impaired vascular remodeling, showed signs of ovarian aging a decade after pregnancy compared with women with normotensive pregnancies⁵². This result has also been confirmed by a study showing that Type 1 diabetes mediated vascular remodeling leads to ovarian aging⁵³. Therefore, the experimental data indicate a pivotal contribution of vascular remodeling in ovarian aging.

In summary, this study provides the first spatiotemporal single-cell transcriptomic atlas of human ovaries during aging and maps discrete sets of cell-type-specific aging regulated genes and core transcription factor FOXP1 that help elucidate the complex biology of human ovarian aging. Importantly, it provides insights into the molecular mechanisms underlying ovarian aging in humans and lays a foundation for the quantitative assessment of the reproductive age of females. Moreover, our study also established new avenues for developing targeted senescent cell interventions to protect against physiological ovarian aging.

Methods

Samples and Ethical Statement

Human ovaries were donated from 9 women underwent oophorectomy because of cervical cancer or carcinoma of endometrium. The sample collection was approved by the Tongji Hospital, Tongji Medical College, Huazhong University of Science and Technology (TJ-IRB20210319). All women have signed informed consents.

Single Cell Isolation

Ovary tissues were saved in tissue storage solution (Miltenyi, 130-100-008) at ice bath and transferred to laboratory within two hours. Then we get rid of damaged parts in light microscopy and cut out a ~ 1 cm³ piece for isolation. The tissue was washed with PBS (containing 0.04% BSA) and cut into 0.1 cm³ in 2 mg/ml IV collagenase. After that the tube containing IV collagenase and tissues was oscillated in water bath at 37°C for 20 min. After centrifuged for 5 min on 1200 rpm the supernatant was discarded and resuspended in 0.5% trypsin. Then the tissues in 0.5% trypsin were oscillated in water bath at 37°C for 15–20 min again. Digestion was stopped with DMEM containing 10% BSA and filtered with 40 µm cell strainer (Millipore) and centrifuged for 5 min on 1200 rpm. Finally cells were incubated in red blood lysis buffer for 10 min then centrifuged and resuspended in 100–200 µL PBS containing 0.04% BSA.

RNA-sequencing on the 10× Genomics platform

Single-cell suspension for each ovary sample was loaded onto a separate channel of a Chromium 10x Genomics single cell 3'v3 library chip as per manufacturer's protocol. cDNA sequencing libraries were prepared according to the manufacturer's protocol and sequenced on an Illumina Novaseq 6000 (2x150bp paired-end reads).

Sequencing Analysis

Raw sequence reads in FASTQ format from ovary samples were processed and aligned to the GRCh38 human reference transcriptome (<https://www.10xgenomics.com/>) using the Cellranger v4.0.0 pipeline (<https://www.10xgenomics.com/>) with default parameters. The resulting gene expression matrices merged together using Seurat package v3⁵⁴. The pre-processing followed the guidelines provided by Seurat V3 tutorial. In short, entries with fewer than 200 genes and greater than 9000 total genes were filtered to remove empty droplets and probable doublets, respectively, and cells that have > 10% mitochondrial counts were also filtered to remove low quality cells. To account for differences in sequencing depth across samples, we normalized expression values for total unique molecular identifiers (UMIs) per cell and log transformed the counts using Seurat Normalize Data function.

Clustering and identification of cell types

All clustering analyses were done followed the Seurat V3 intergrated tutorial .The first 30 principal components were used for PCA (Principal component analysis). Clustering was performed using the FindClusters function, which works on K-nearest neighbor (KNN) graph model with the granularity 0.5 and were displayed in UMAP/t-SNE plots. FindAllMarkers function in Seurat was performed to call cell type-specific genes with default parameter. Cell type of each cluster was identified by known marker genes. For each cell type, we rerun the Seurat cluster workflow to identify cell sub-types.

Analysis of DEGs and GO and pathway enrichment analysis

FindMarkers function in Seurat was used to call differentially expressed genes between Young Middle and Old with default parameter. GO enrichment for DEGs was done by using TopGO package in R. KEGG Pathway information was download from KEGG website, and enricher function in ClusterProfiler package was used to analysis KEGG enrichment.

Identification of Aging-Associated and age-dependent DEGs

We used the function of "FindMarkers" in Seurat to identify aging-associated differentially expressed genes (DEGs) between the old and young groups (O/Y), middle-aged and young groups (M/Y), and old and middle-aged groups (O/M) for each cell type. The log fold change (LogFC) and adjusted p value of each DEG were calculated by using the non-parametric two-sided Wilcoxon rank-sum test and only those with $|'avg_logFC'| > 0.25$ were considered to be aging-associated DEGs

To identify age-dependent DEGs, we used the function of "FindAllMarkers" in Seurat to identify age-dependent DEGs of different ages for each cell type. The log fold change (LogFC) of each DEGs and the adjusted p value were tested by nonparametric bilateral Wilcoxonrank sum test. Only those with $|'avg_logFC'| > 0.25$ were considered as age-dependent DEGs. We used the age-dependent DEGs calculated to define an expression matrix, and the cells of each cell type are sorted by age scale. The heatmap package was then used to visualize the spline smooth expression pattern of age-dependent genes with the parameters "hclust_method = 'ward.D2'".

Gene set score analysis

The “AddModuleScore” function in Seurat was used to calculate module scores for gene expression programs in single cells. First, all the analyzed genes are binned based on the average expression, and the control genes are randomly selected from each bin. Then, calculate the average expression value of the gene set at the single-cell level minus the aggregated expression of the control gene set. Gene sets were obtained from the MSigDB database (<https://www.gsea-msigdb.org/gsea/msigdb/>) and are listed in Table S6.

Pseudotime Analysis

R package Monocle2⁵⁵ (version 2.99.3) was used to reconstruct the epidermal cell developmental trajectory. The UMIs matrix was used as input and variable genes obtained from epidermal cell types were detected by Seurat to sort cells in pseudotime.

Transcriptional Regulatory Network Analysis

The transcriptional regulatory network was analyzed by the PYSCENIC workflow using default parameters. Transcription factors (TFs) of hg38 were used as reference TFs and downloaded from RcisTarget(<https://resources.aertslab.org/cistarget/>). The gene expression matrix of all celltypes were normalized from Seurat as input. Firstly, co-expression modules were identified between TFs and the potential target genes based on the gene expression matrix through grnboost2 module. Secondly, for each co-expression module, the cis-regulatory motif enrichment analysis was performed among all potential target genes by ctx module, and only the target genes enriched with the motifs of the corresponding TFs were selected as direct target genes. Each transcription factor and its direct target genes were defined as a regulon. Finally, Regulon specificity scores (RSS) was calculated for each cell. Networks of the TF modules were visualized by Cytoscape (version 3.8.2).

Tissue preparation for Spatial Transcriptomics

Ovary tissues were obtained and transported to laboratory as above. Then, the samples were cut into 6 mm³ piece and dried with lab blotting paper to prevent ice crystal formation. After that we embedded the tissue with OCT into the embedding box in dry ice and saved in -80 °C.

Spatial transcriptomic data processing

We used Space Ranger V1.2.1 to process raw fastq files. The Space Ranger output files were then imported into R environment (V4.0.5) and analysed using R package Seurat v4.0.1 (<https://github.com/satijalab/seurat/>). We obtained information about the number of spots, UMIs under each tissue, and median/mean genes and reads per spot, etc. SCTransform was used to normalize data followed by PCA. The spatial expression of selected genes were visualized by the using the normalized data. The spatial expression of selected Gene sets from the MSigDB database (<https://www.gsea-msigdb.org/gsea/msigdb/>) was visualized by R package SPATA2 V0.1.0 (<https://themilolab.github.io/SPATA2/>).

Cell-type annotation of the Spatial transcriptomic data

To obtain cell-type annotation of the Slide-seq datasets, the annotated single-cell RNA-seq dataset for the same tissue from the identical person were used as reference dataset. The single-cell RNA-seq dataset was also normalized by SCTransform followed by PCA. Cell-type annotation was performed using the Seurat cell-type annotation pipeline with function FindTransferAnchors setting parameter "normalization.method = 'SCT'", and function TransferData setting parameters "prediction.assay = 'TRUE'" and "dims = '1:30'".

In order to further splitting Granulosa cells (or Theca & stroma cells) into subclusters, spots containing these cells were clustered into several groups according to their cell-type annotation. For echo group, we filtered the original single-cell reference dataset by cell-type annotation to get a new dataset with the same cell-type using Seurat function subset. The Seurat cell-type annotation pipeline were performed for echo spot groups respectively with the cells of Granulosa cells (or Theca & stroma cells) relabeled with the subtype names.

Differential expression analysis of anatomical regions

We selected the Spots of specific anatomical regions using the function pl.het_plot_interactive of stlearn v0.3.2 (<https://github.com/BiomedicalMachineLearning/stLearn>). We used FindMarkers function to perform differential gene expression analysis between regions and set p_val_adj = 0.05 as the cutoff value. DEGs were visualized as heatmap with the R package ComplexHeatmap. GO analysis of these DEGs was performed by Metascape (Zhou et al., 2019) (version 3.5, <http://metascape.org/>) and selected pathway terms were displayed in the heatmap.

Spatial trajectories analysis

We performed spatial trajectories analysis following the tutorial of SPATA2 (<https://themilolab.github.io/SPATA2/articles/spata-v2-trajectory-analysis.html>) to find genes that followed a certain trend along the trajectory of interest. We extracted genes fit against any of the predefined models to a quality-degree i.e. auc-evaluations equal to or lower than 3. Instead of visualizing using the original plotTrajectoryHeatmap function of SPATA2, we modified the final heatmap plotting codes of the function with the R package ComplexHeatmap.

Hematoxylin and eosin staining

Tissues were dipped in 4% paraformaldehyde and paraffin-embedded then sectioned in a 4- μ m thickness. For staining, sections were dried at 65°C for 1.5 h and dewaxed in environmental protection dewaxing transparent liquid (Servicebio, China) for 40 min. Then successively dipped in 100%, 90%, 80%, 70% ethyl alcohol for 10 min, 10 min, 5 min, 5 min. After incubated sections in ultrapure water for 10 min, we dropped them in hematoxylin solution (Servicebio, China) for 3 min and washed away residual dye. Then sections were rinsed in hydrochloric acid alcohol for 1–3 s and washed in running water for a moment.

Finally, we incubated sections in eosin for 3–5 min and in 100%, 90%, 80%, 70% ethyl alcohol in order for 5 min, 5min, 10 min, 10 min.

Immunofluorescence

After de-paraffinization and rehydration, sections were conducted antigen retrieval using EDTA Antigen repair Buffer (PH9.0) at 100°C for 23 min. Then we washed sections in PBS 3 times for 5 min each. After blocking with 5% BSA for 30 min at 37°C, sections were incubated in primary antibodies at 4°C overnight. The antibodies were listed as follows: AMH (14461-1-AP, 1:100), GSTA1 (A18266, 1:50), ZP3 (21279-1-AP, 1:50), TUBB8 (A12617, 1:50), P21 (10355-1-AP:1:100), CD31 (ab9498, 1:100), α -SMA (ab124964, 1:1000), Ki67 (27309-1-AP, 1:100), γ -H2AX (AP0099, 1:100). The next day, sections were washed in PBS three times and then incubated in Donkey anti Rabbit IgG(H + L)(1:200 dilution) (Antgene, China) for 1 h at 37°C away from light. Finally, sections were stained with DAPI for 5 min and examined with BX51 microscope (Olympus Corporation, Japan).

Lipofuscin staining

0.15 g Sudan black B (Solarbio, China) were dissolved in 100 mL 70% ethyl alcohol and stored sealed away from light. Before using for lipofuscin staining, Sudan black B dye liquor was filtered with filter paper. Frozen sections of human ovaries were balanced at room temperature for at least 30 min. Then sections were incubated in 1% methanol (dilute) for 5 min and incubated in PBS twice for 5 min, then 50% and 70% ethyl alcohol for 5 min. Afterword, filtered Sudan black B dye liquor was dropped in sections for 5–10 min and washed in 50% ethyl alcohol and then ultrapure water. Finally sections were incubated with nuclear solid red for 5 min and examined by microscopic (CX43, Olympus, Japan).

RNA isolation and RT-qPCR

Total RNA was exacted with TRIzol Reagent (Invitrogen, USA). After assessing the concentration of RNA with Nanodrop 2000 ultra-microspectrophotometer (Thermo, USA), 2 ug total RNA was reverse as cDNA using HiScript® II Q RT SuperMix for qPCR (+ gDNA wiper) kit. RT-qPCR was conducted with ChamQ™ Universal SYBR qPCR master mix bought from Vazyme (R223-01, Q711-02; Nanjing, Jiangsu, China) on the CFX96 real-time PCR system (Bio-Rad). All data were calculated by $2^{-\Delta\Delta Ct}$. Primers are listed in Table S7.

Cell culture and treatment

COV434 cells and primary theca & stroma cells were transfected with siRNA (RIBOBIO, China) targeting FOXP1, SOX4, and FOS using Lipofectamine 3000 (Thermo, L3000015). Sequences of the siRNAs were listed in Table S7. In brief, cells were incubated in 50 nM siRNAs for 6 h and cultured in DMEM containing 10% FBS for another 48h. After that, cells were sacrificed for RT-PCR, Western blot, SA- β -Gal staining and immunofluorescence.

Chromatin immunoprecipitation

Chromatin immunoprecipitation (ChIP) was conducted with COV434 cells using the SimpleChIP Enzymatic Chromatin IP Kit (Magnetic Beads) (Cell Signaling Technology). In brief, chromatin was cross-linked by 1% formaldehyde and digested with micrococcal nuclease. FOXP1 antibody, normal rabbit IgG, and Protein G Magnetic Beads were used to precipitate specific chromatin fragments. DNA fragments were purified using DNA purification spin columns after reverse cross-linking of the DNA/protein complex. Enrichment of DNA sequences was determined by quantitative realtime PCR. The primers used for ChIP-PCR are listed in Table S7.

Oil Red staining

Frozen sections of human ovaries were taken out from -80°C and balanced in room temperature for at least 30 min. Saturated oil red O dye A was diluted with ddH₂O in 3:2 and filtered with filter paper. Then sections were incubated in dye liquor away from light for 10 min. After washed with ddH₂O two times, sections were stained with hematoxylin staining solution for 3 min and finally examined by microscopic.

Masson staining

After de-paraffinization and rehydration, sections were incubated in potassium dichromate overnight. Hematoxylin iron A and B were equal-ratio mixture into the dye of ferric hematoxylin. Then sections were stained with above commixture for 3 min, Richun red acid magenta for 10 min, phosphomolybdic acid aqueous solution for 3 min and aniline blue dye for 5 min. Finally sections were dehydrated in absolute ethyl alcohol and examined by microscopic.

SA- β -Gal staining

Cells were seeded into 6-well plates and treated as above. For SA- β -Gal staining, we used Senescence β -Galactosidase Staining Kit (Beyotime Biotechnology, China). In brief, cells were washed with PBS and incubated in stationary liquid for 15 min at room temperature. After washed in PBS 3 times for 3 minutes each, cells were incubated in dyeing working fluid for 10–14 h in 37°C without CO₂. The next day, dyeing working fluid was discarded and washed with PBS 3 times then stored in PBS. Finally sections were examined in microscopic (CX43, Olympus, Japan).

Statistical analyses

Data in bar plots are shown as the mean \pm SEM. All experimental data were analyzed using unpaired t test or Oneway analysis of variance (ANOVA) to compare differences between groups (GraphPad 9.0 Software). *P value < 0.05 was considered to be statistically significant. Blank indicates not significant. Spearman's rank correlation coefficient (r) were used to calculate correlation associated statistical significance in GraphPad 9.0 Software.

Declarations

ACKNOWLEDGMENTS

This work was financially supported by the National Natural Science Foundation of China (no. 81873824, 82001514, 82001498, 8210062421, 22104040) and the Fundamental Research Funds for the Central Universities (HSUT: 2021yjsCXCY087). Part of the bioinformatics analysis was performed on the computing platform of the Personalbio.

AUTHOR CONTRIBUTIONS

S.W. and M.W. conceptualized this project and supervised the overall experiments. M.W., W.T., and Y.C. performed isolation of ovarian cells. W.T., Y.C., C.W., and X.Z. performed ovary histological analysis. W.T., Y.C., D.C., L.X., J.X., Y.G. and Y.H. performed cell culture as well as functional and mechanistic analyses. Y.Z. and H.L. performed bioinformatics analysis of the scRNA-seq and ST-seq data. C.S., Y.L., J.Z., J.D., S.Z., Q.Z., S.W., J.Y., J.G., M.F. W., Y.L., T.X. and S.W. performed manuscript writing, review, and editing.

DECLARATION OF INTERESTS

The authors declare no competing interests.

References

1. Baerwald, A.R., Adams, G.P. & Pierson, R.A. Ovarian antral folliculogenesis during the human menstrual cycle: a review. *Human reproduction update* **18**, 73–91 (2012).
2. Broekmans, F.J., Knauff, E.A., te Velde, E.R., Macklon, N.S. & Fauser, B.C. Female reproductive ageing: current knowledge and future trends. *Trends in endocrinology and metabolism: TEM* **18**, 58–65 (2007).
3. Laisk, T. *et al.* Demographic and evolutionary trends in ovarian function and aging. *Human reproduction update* **25**, 34–50 (2019).
4. Broekmans, F.J., Soules, M.R. & Fauser, B.C. Ovarian aging: mechanisms and clinical consequences. *Endocr Rev* **30**, 465–493 (2009).
5. Hsueh, A.J., Kawamura, K., Cheng, Y. & Fauser, B.C. Intraovarian control of early folliculogenesis. *Endocrine reviews* **36**, 1–24 (2015).
6. Tabula Muris, C. A single-cell transcriptomic atlas characterizes ageing tissues in the mouse. *Nature* **583**, 590–595 (2020).
7. Fan, X. *et al.* Single-cell reconstruction of follicular remodeling in the human adult ovary. *Nature communications* **10**, 3164 (2019).
8. Wagner, M. *et al.* Single-cell analysis of human ovarian cortex identifies distinct cell populations but no oogonial stem cells. *Nature communications* **11**, 1147 (2020).

9. Eng, C.L. *et al.* Transcriptome-scale super-resolved imaging in tissues by RNA seqFISH. *Nature* **568**, 235–239 (2019).
10. Chen, K.H., Boettiger, A.N., Moffitt, J.R., Wang, S. & Zhuang, X. RNA imaging. Spatially resolved, highly multiplexed RNA profiling in single cells. *Science* **348**, aaa6090 (2015).
11. Salmen, F. *et al.* Barcoded solid-phase RNA capture for Spatial Transcriptomics profiling in mammalian tissue sections. *Nature protocols* **13**, 2501–2534 (2018).
12. Feng, R. *et al.* Mutations in TUBB8 and Human Oocyte Meiotic Arrest. *The New England journal of medicine* **374**, 223–232 (2016).
13. Zhao, M., Chen, L. & Qu, H. CSGene: a literature-based database for cell senescence genes and its application to identify critical cell aging pathways and associated diseases. *Cell death & disease* **7**, e2053 (2016).
14. Georgakopoulou, E.A. *et al.* Specific lipofuscin staining as a novel biomarker to detect replicative and stress-induced senescence. A method applicable in cryo-preserved and archival tissues. *Aging* **5**, 37–50 (2013).
15. Secomandi, L., Borghesan, M., Velarde, M. & Demaria, M. The role of cellular senescence in female reproductive aging and the potential for senotherapeutic interventions. *Human reproduction update* (2021).
16. Ruth, K.S. *et al.* Genetic insights into biological mechanisms governing human ovarian ageing. *Nature* **596**, 393–397 (2021).
17. Peng, J.Y. *et al.* Molecular cloning, expression analysis, and function of decorin in goat ovarian granulosa cells. *Domestic animal endocrinology* **57**, 108–116 (2016).
18. Kedem, A. *et al.* Elucidating Decorin's role in the preovulatory follicle. *Journal of ovarian research* **13**, 15 (2020).
19. Hummitzsch, K. *et al.* Transcriptome analyses of ovarian stroma: tunica albuginea, interstitium and theca interna. *Reproduction* **157**, 545–565 (2019).
20. Kuilman, T., Michaloglou, C., Mooi, W.J. & Peeper, D.S. The essence of senescence. *Genes & development* **24**, 2463–2479 (2010).
21. Di Micco, R., Krizhanovsky, V., Baker, D. & d'Adda di Fagagna, F. Cellular senescence in ageing: from mechanisms to therapeutic opportunities. *Nature reviews. Molecular cell biology* **22**, 75–95 (2021).
22. Brown, H.M. & Russell, D.L. Blood and lymphatic vasculature in the ovary: development, function and disease. *Human reproduction update* **20**, 29–39 (2014).
23. Levi, N., Papismadov, N., Solomonov, I., Sagi, I. & Krizhanovsky, V. The ECM path of senescence in aging: components and modifiers. *FEBS J* **287**, 2636–2646 (2020).
24. Wang, S. *et al.* Single-Cell Transcriptomic Atlas of Primate Ovarian Aging. *Cell* **180**, 585–600 e519 (2020).
25. Rogers, J. & Gibbs, R.A. Comparative primate genomics: emerging patterns of genome content and dynamics. *Nature reviews. Genetics* **15**, 347–359 (2014).

26. Zhang, Z.D., Frankish, A., Hunt, T., Harrow, J. & Gerstein, M. Identification and analysis of unitary pseudogenes: historic and contemporary gene losses in humans and other primates. *Genome biology* **11**, R26 (2010).
27. Llonch, S. *et al.* Single human oocyte transcriptome analysis reveals distinct maturation stage-dependent pathways impacted by age. *Aging cell* **20**, e13360 (2021).
28. Lieber, M.R. & Karanjawala, Z.E. Ageing, repetitive genomes and DNA damage. *Nature reviews. Molecular cell biology* **5**, 69–75 (2004).
29. Gorbunova, V., Seluanov, A., Mao, Z. & Hine, C. Changes in DNA repair during aging. *Nucleic acids research* **35**, 7466–7474 (2007).
30. Adhikari, D. & Liu, K. Molecular mechanisms underlying the activation of mammalian primordial follicles. *Endocrine reviews* **30**, 438–464 (2009).
31. Maidarti, M., Anderson, R.A. & Telfer, E.E. Crosstalk between PTEN/PI3K/Akt Signalling and DNA Damage in the Oocyte: Implications for Primordial Follicle Activation, Oocyte Quality and Ageing. *Cells* **9** (2020).
32. Grondahl, M.L. *et al.* Gene expression profiles of single human mature oocytes in relation to age. *Human reproduction* **25**, 957–968 (2010).
33. Suh, E.K. *et al.* p63 protects the female germ line during meiotic arrest. *Nature* **444**, 624–628 (2006).
34. Kerr, J.B. *et al.* DNA damage-induced primordial follicle oocyte apoptosis and loss of fertility require TAp63-mediated induction of Puma and Noxa. *Molecular cell* **48**, 343–352 (2012).
35. Winship, A.L., Stringer, J.M., Liew, S.H. & Hutt, K.J. The importance of DNA repair for maintaining oocyte quality in response to anti-cancer treatments, environmental toxins and maternal ageing. *Human reproduction update* **24**, 119–134 (2018).
36. Griffin, J., Emery, B.R., Huang, I., Peterson, C.M. & Carrell, D.T. Comparative analysis of follicle morphology and oocyte diameter in four mammalian species (mouse, hamster, pig, and human). *Journal of experimental & clinical assisted reproduction* **3**, 2 (2006).
37. Calcinotto, A. *et al.* Cellular Senescence: Aging, Cancer, and Injury. *Physiological reviews* **99**, 1047–1078 (2019).
38. Riessland, M. *et al.* Loss of SATB1 Induces p21-Dependent Cellular Senescence in Post-mitotic Dopaminergic Neurons. *Cell stem cell* **25**, 514–530 e518 (2019).
39. Ansere, V.A. *et al.* Cellular hallmarks of aging emerge in the ovary prior to primordial follicle depletion. *Mechanisms of ageing and development* **194**, 111425 (2021).
40. Lin, X. *et al.* Excessive oxidative stress in cumulus granulosa cells induced cell senescence contributes to endometriosis-associated infertility. *Redox biology* **30**, 101431 (2020).
41. Munoz-Espin, D. & Serrano, M. Cellular senescence: from physiology to pathology. *Nature reviews. Molecular cell biology* **15**, 482–496 (2014).
42. Wang, B. *et al.* Foxp1 regulates cardiac outflow tract, endocardial cushion morphogenesis and myocyte proliferation and maturation. *Development* **131**, 4477–4487 (2004).

43. Shu, W. *et al.* Foxp2 and Foxp1 cooperatively regulate lung and esophagus development. *Development* **134**, 1991–2000 (2007).
44. Feng, X. *et al.* Transcription factor Foxp1 exerts essential cell-intrinsic regulation of the quiescence of naive T cells. *Nature immunology* **12**, 544–550 (2011).
45. Li, H. *et al.* FOXP1 controls mesenchymal stem cell commitment and senescence during skeletal aging. *The Journal of clinical investigation* **127**, 1241–1253 (2017).
46. Ruan, L., Xie, Y., Liu, F. & Chen, X. Serum miR-1181 and miR-4314 associated with ovarian cancer: MiRNA microarray data analysis for a pilot study. *European journal of obstetrics, gynecology, and reproductive biology* **222**, 31–38 (2018).
47. Libby, P. Inflammation in atherosclerosis. *Nature* **420**, 868–874 (2002).
48. Childs, B.G., Durik, M., Baker, D.J. & van Deursen, J.M. Cellular senescence in aging and age-related disease: from mechanisms to therapy. *Nat Med* **21**, 1424–1435 (2015).
49. Binet, F. *et al.* Neutrophil extracellular traps target senescent vasculature for tissue remodeling in retinopathy. *Science* **369** (2020).
50. Kok, H.S. *et al.* Heart disease risk determines menopausal age rather than the reverse. *J Am Coll Cardiol* **47**, 1976–1983 (2006).
51. Appt, S.E., Chen, H., Clarkson, T.B. & Kaplan, J.R. Premenopausal antimullerian hormone concentration is associated with subsequent atherosclerosis. *Menopause* **19**, 1353–1359 (2012).
52. Yarde, F. *et al.* Serum AMH levels in women with a history of preeclampsia suggest a role for vascular factors in ovarian aging. *J Clin Endocrinol Metab* **99**, 579–586 (2014).
53. Yarde, F. *et al.* Association between vascular health and ovarian ageing in type 1 diabetes mellitus. *Hum Reprod* **31**, 1354–1362 (2016).
54. Stuart, T. *et al.* Comprehensive Integration of Single-Cell Data. *Cell* **177**, 1888–1902 e1821 (2019).
55. Qiu, X. *et al.* Reversed graph embedding resolves complex single-cell trajectories. *Nature methods* **14**, 979–982 (2017).

Figures

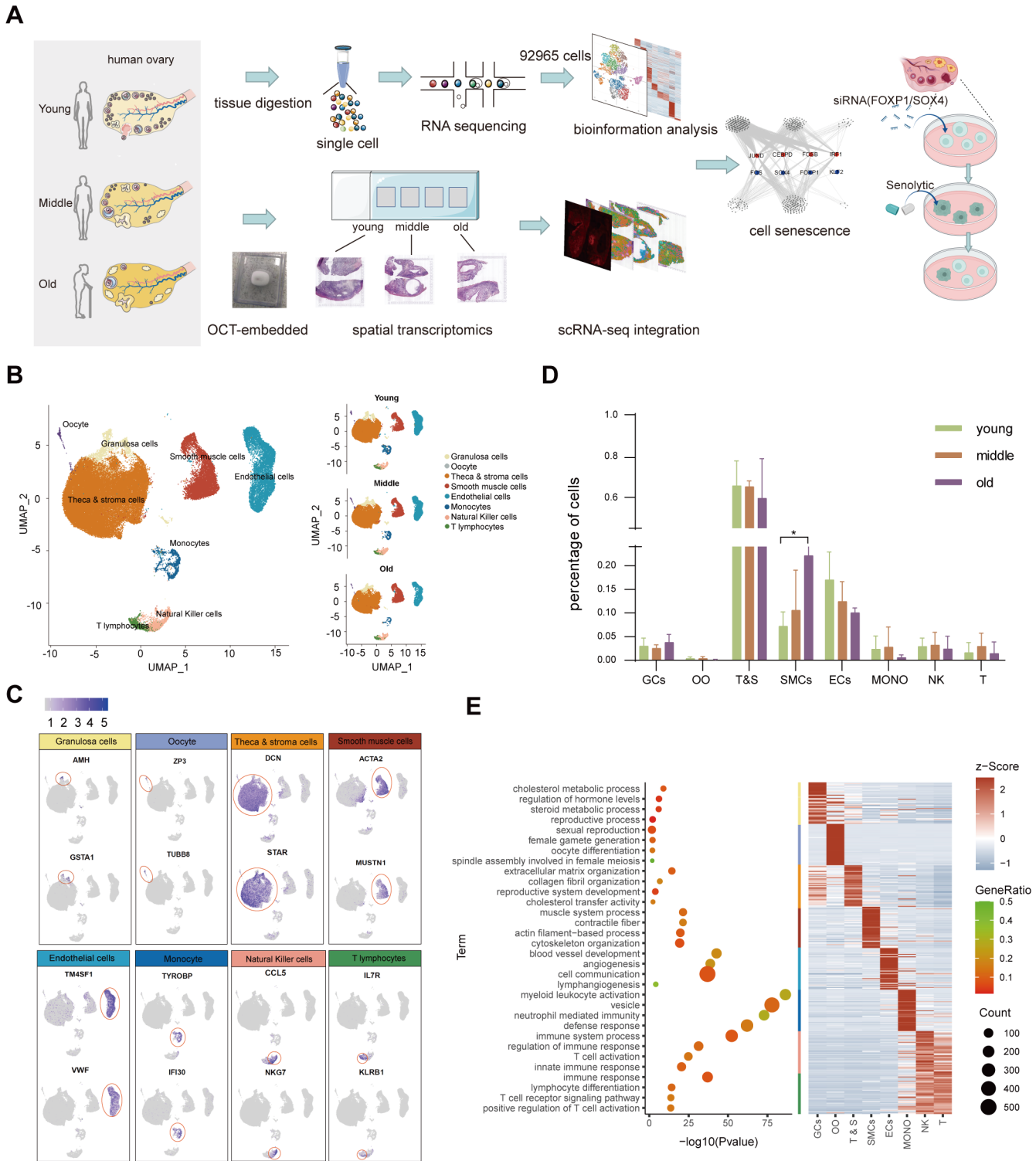


Figure 1

The Transcriptional Atlas of Human Ovarian Aging by Single-Cell RNA-Seq Analysis.

(A) Study flowchart.

(B) UMAP plots showing eight cell types (left) and age-dependent cell distribution (right).

(C) UMAP cluster map of each slide showing expression of marker genes. The cell clusters are circled in red.

(D) Histogram showing percentage of each cell type between three groups. Data are presented as the mean \pm SEM. n = 3 for each group. *p < 0.05.

(E) Left: representative GO terms of different cell types. Right: heatmap showing top 50 marker genes in each cell type.

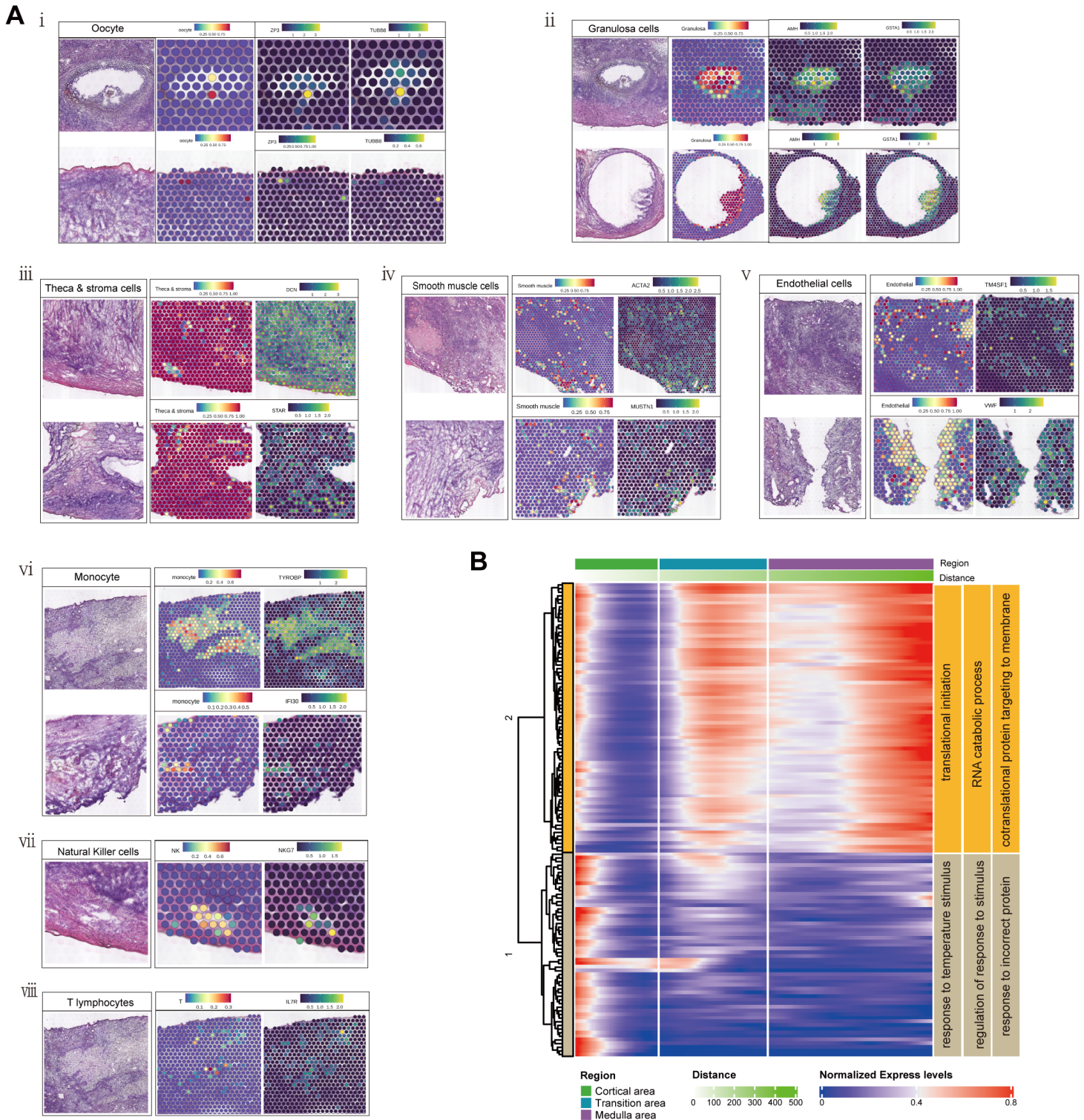


Figure 2

Spatial Analysis of Human Ovaries with Integration of ST and scRNA-seq.

(A) Each slide (i-viii) showing H&E staining, ST spot cell type predictions and characteristic markers respectively of each cell type from left to right. The scale color from blue to red represents the expression level.

(B) Heatmap showing distance dependent expression of genes that vary much significantly with different distance. The distance of ovarian surface is zero and the inner, the greater the distance. Specific GO terms are listed on the right.

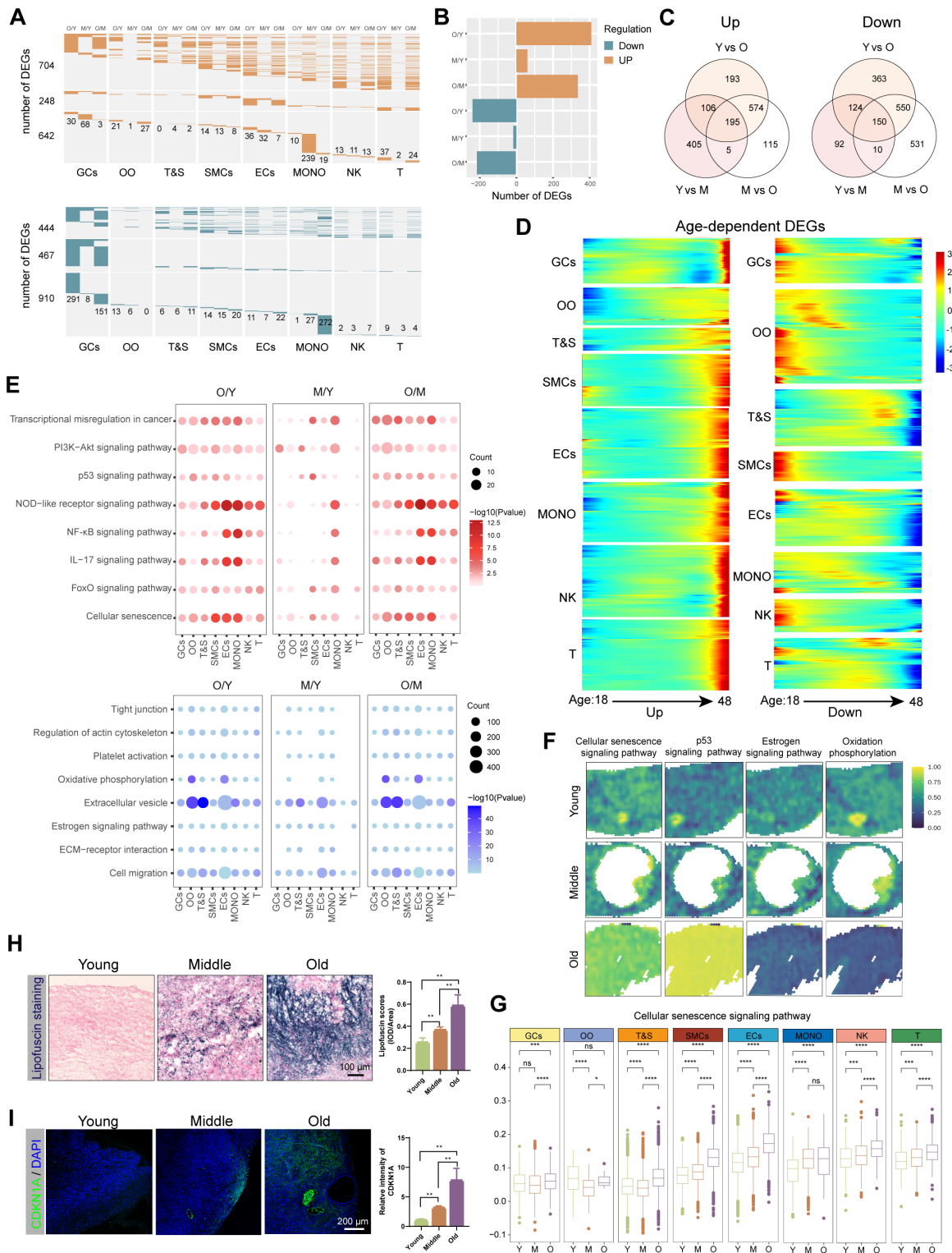


Figure 3

Changes of the Transcriptional Profiles of Different Cell Types during Human Ovarian Aging.

(A) Heatmaps showing the upregulated (upper) and downregulated (below) DEGs of each cell type between the old and young groups (O/Y), middle and young groups (M/Y), and old and middle groups (O/M). Gene numbers on the left represents from top to bottom, DEGs shared by at least two cell types, DEGs shared by at least two groups, unique DEGs of each cell type in each group. The numbers of unique DEGs are annotated.

(B) Total numbers of DEGs between the old and young groups (O/Y), middle and young groups (M/Y), and old and middle groups (O/M).

(C) Venn diagram of DEGs shared by three groups.

(D) Heatmaps showing the age-dependent DEGs of eight ovarian cell types. The color key from blue to red represents low to high gene expression levels.

(E) Representative KEGG pathways of upregulated DEGs (upper) and downregulated DEGs (below) compared between three groups in different cell types. "Count" indicates gene numbers. The color from gray to red (up), or from gray to blue (down), indicate the p value.

(F) ST spot illustrating representative KEGG pathways within ovarian aging. The color key from blue to yellow indicates low to high enrichment levels.

(G) Gene set score analysis of cell senescence pathways in various ovarian cell types of different groups. Y, young; M, middle; O, old. ns, not significant; * $p < 0.05$; *** $p < 0.001$; **** $p < 0.0001$; (two-sided Wilcoxon rank-sum tests).

(H) Lipofuscin staining of different aged human ovaries. Scale bar, 100 μm . Data are presented as the mean \pm SEM. $n = 3$ for each group. ** $p < 0.01$.

(I) Immunofluorescence staining of CDKN1A of different aged human ovaries. Scale bar, 200 μm . Data are presented as the mean \pm SEM. $n = 3$ for each group. ** $p < 0.01$.

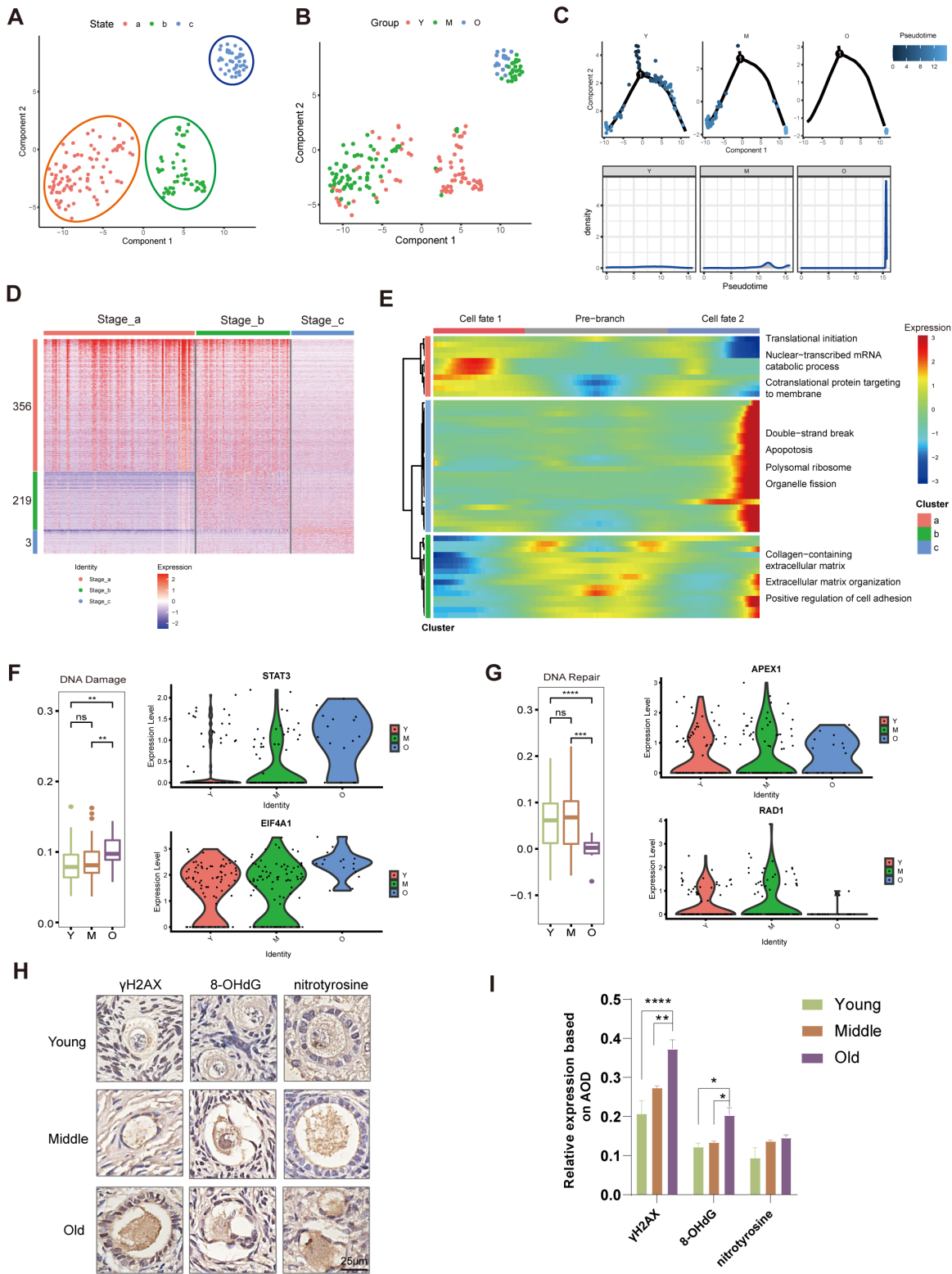


Figure 4

Changes of Oocyte within Ovarian Aging.

(A)(B) Pseudotime trajectory plot (left) and UMAP plot (right) illustrating distribution of oocytes.

(C) 2D graph of the pseudotime-ordered oocyte cells, from young, middle and old groups.

(D) Heatmap illustrating the DEGs of each stage during oocyte aging. DEG numbers are shown on the left.

(E) Heatmap showing the dynamic DEGs along the pseudotime. The related biological process of each sub-types is listed on the right.

(F) Gene set score analysis of DNA damage pathways in oocytes of different groups. Representative genes are exhibited on the right.

(G) Gene set score analysis of DNA repair pathways in oocytes of different groups. Representative genes are exhibited on the right.

(H) Representative images of oocytes by IHC of γ H2AX, 8-OHdG and nitrotyrosine between three groups. Scale bar, 25 μ m.

(I) IHC scores of relative expression for each group. Data are presented as the mean \pm SEM. n = 4 for each group. *p < 0.05; **p < 0.01; ****p < 0.0001.

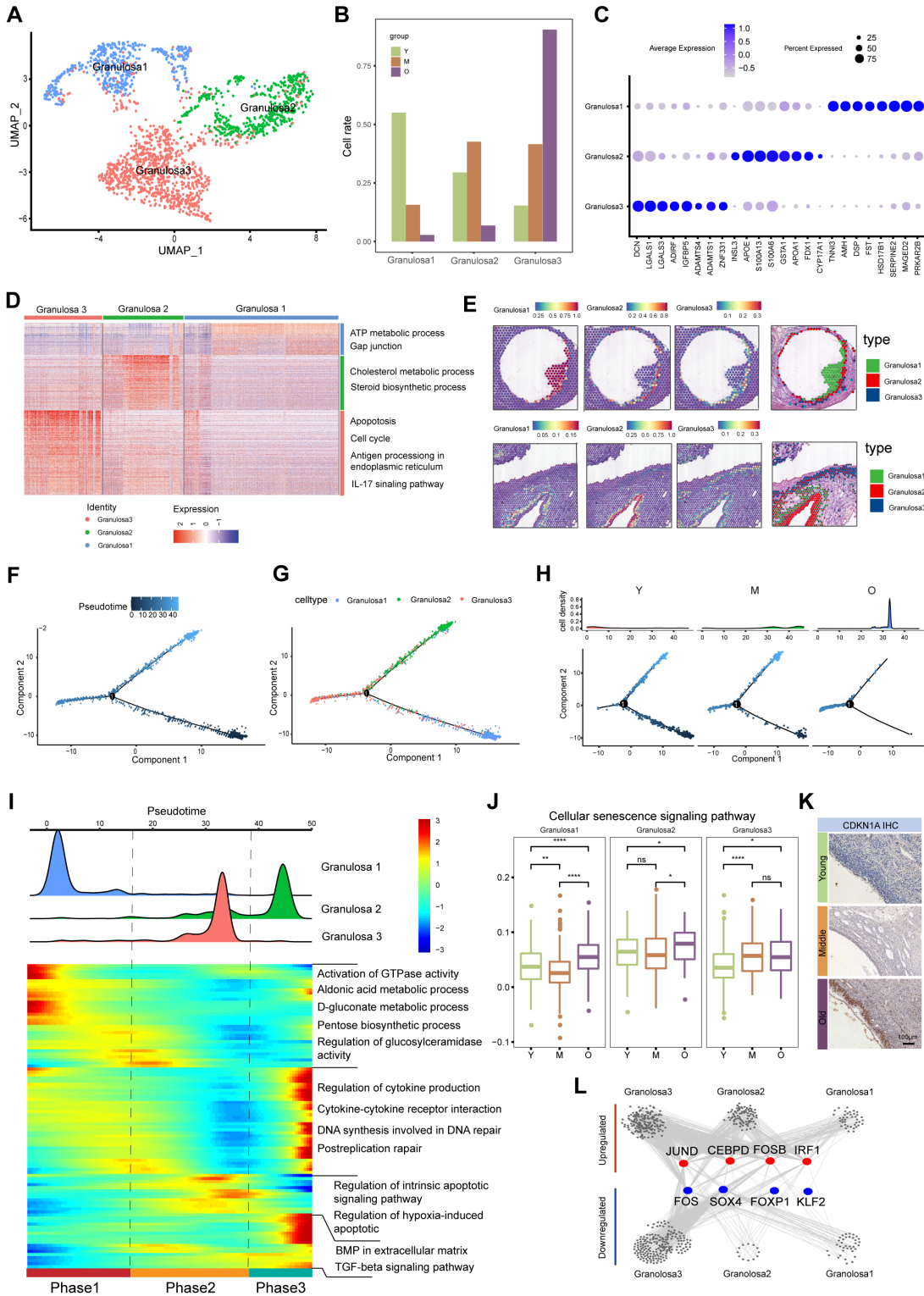


Figure 5

Subpopulations of Human Granulosa Cells and Changes with Age.

(A) UMAP visualization of granulosa cells sub-clusters.

- (B) Histogram showing the cell rate of three granulosa cells sub-clusters, in young, middle and old groups.
- (C) Dot plot heatmap showing top 8 sub-cluster markers.
- (D) Heatmap showing the highly expressed genes specifically in granulosa 1, granulosa 2, granulosa 3.
- (E) The spatial cluster distribution of each sub-clusters (left) and ST spot overlapped with H&E staining (right). The above and below represent different samples respectively.
- (F) Pseudotime-ordered analysis of granulosa cells.
- (G) Granulosa cells subtypes are labeled by colors.
- (H) 2D graph of the pseudotime-ordered granulosa cells, from young, middle and old groups. The cell density distribution is shown above the figure.
- (I) Heatmap showing the dynamic DEGs along the pseudotime. According to the highly expressed genes, the distribution of GCs subtypes is divided into 3 phases. Subtypes are labeled by colors (upper panel). The related biological process of each sub-types is listed on the right.
- (J) The change of gene set score analysis of cellular senescence pathways in subtypes with age.
- (K) Representative images of anti-CDKN1A of granulosa cells by IHC between three groups. Scale bar, 100 μm .
- (L) Network of regulatory TFs showing upregulated and downregulated core in three granulosa subpopulations. Node size correlates with the number of edges positively.

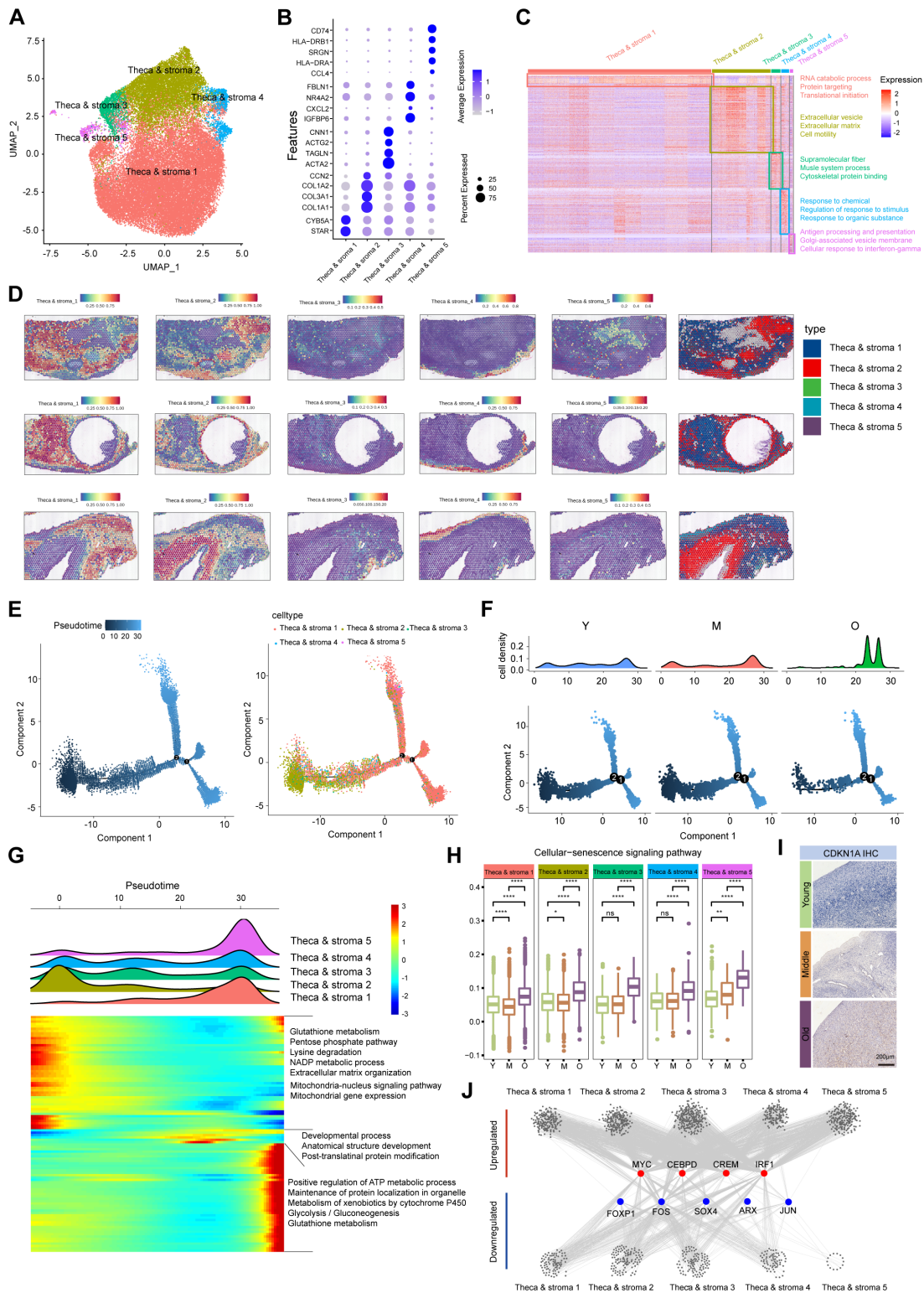


Figure 6

Subpopulations of Human Theca & Stroma Cells and Changes with Age.

(A) UMAP visualization of stroma & theca cells sub-clusters.

(B) Dot plot heatmap showing top sub-cluster markers.

- (C) Heatmap showing the highly expressed genes specifically in theca & stroma 1, theca & stroma 2, and theca & stroma 3, theca & stroma 4, theca & stroma 5.
- (D) The spatial cluster distribution of each sub-clusters (left) and ST spot overlapped with H&E staining (right). The upper, middle and lower represent different samples respectively.
- (E) Pseudotime-ordered analysis of theca & stroma cells (left). Subtypes are labeled by colors (right).
- (F) 2D graph of the pseudotime-ordered theca & stroma cells, from young, middle and old groups. The cell density distribution is shown above the figure.
- (G) Heatmap showing the dynamic DEGs along the pseudotime. According to the highly expressed genes, the distribution of GCs subtypes is divided into 3 phases. Subtypes are labeled by colors (upper panel). The related biological process of each sub-types is listed on the right.
- (H) The change of gene set score analysis of cellular senescence pathways in subtypes with age.
- (I) Representative images of anti-CDKN1A of theca & stroma cells by IHC between three groups. Scale bar, 200 μm .
- (J) Network of regulatory TFs showing upregulated and downregulated core in five theca & stroma subpopulations. Node size correlates with the number of edges positively.

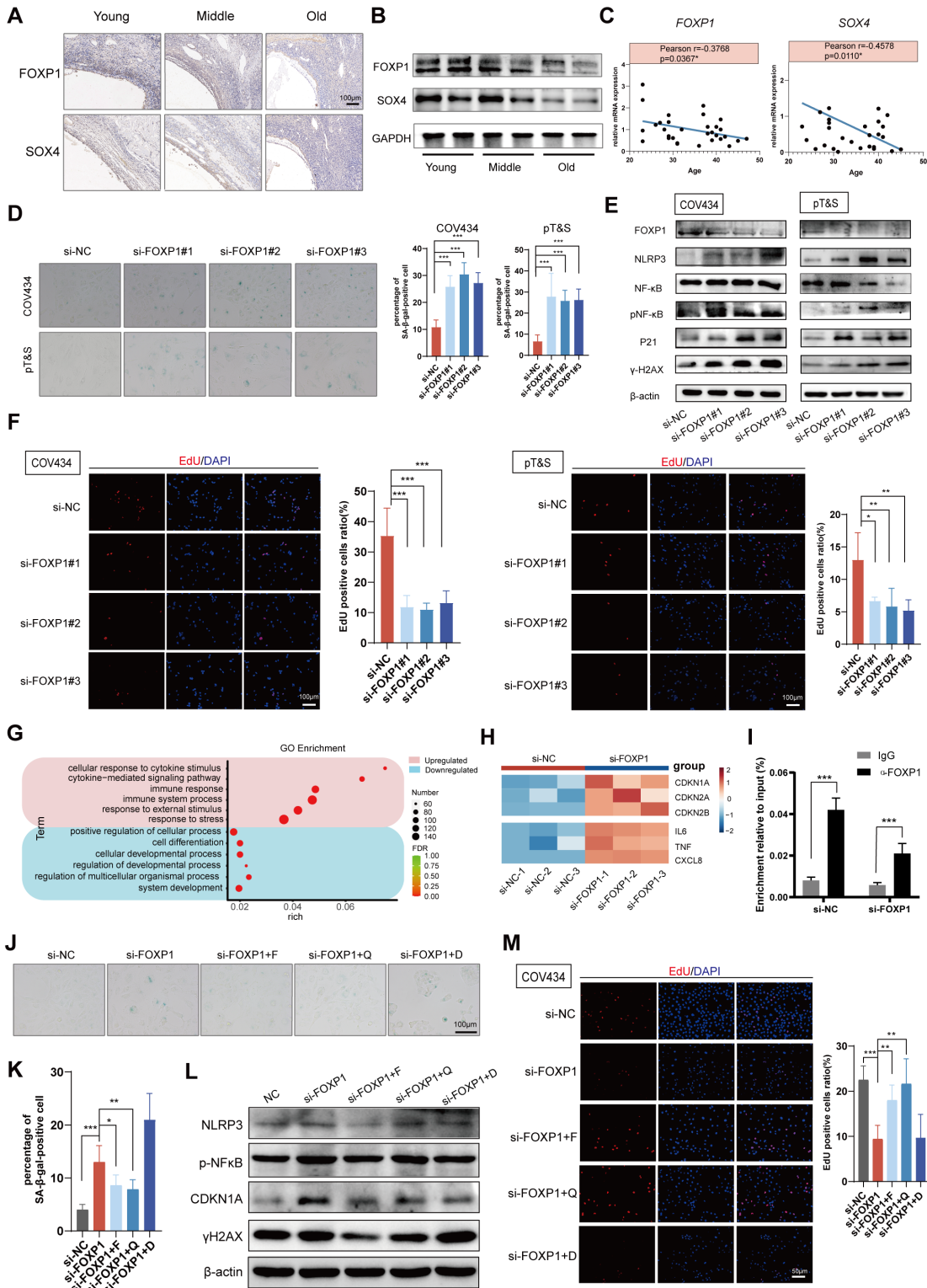


Figure 7

Knockdown of FOXP1 in Human Granulosa Cells and Stromal Cells.

(A) Representative image of IHC analysis of SOX4 and FOXP1 in different human ovaries. Scale bar, 100 µm.

- (B) Western blotting of the SOX4 and FOXP1 protein levels in different aged human ovaries.
- (C) The negative correlation of relative FOXP1 levels (left) and SOX4 levels (right) with age in hGCs. n =30 and 27 respectively.
- (D) SA-β-gal staining in COV434 (a human granulosa cell line) and pT&S (primary theca & stroma cells) upon si-FOXP1-mediated gene knockdown. Scale bar, 100 μm. The percentage of SA β-gal-positive cells are shown on the right. Data are presented as the mean ± SEM. n = 5-8 for each group. ***p < 0.001.
- (E) Relative protein expression of genes related to the Nod-like receptor signaling pathway, NF-kappa B signaling pathway, cellular senescence and DNA damage in COV434 and pT&S upon si-FOXP1-mediated gene knockdown, are detected by Western blot (n=3/group).
- (F) Proliferation of COV434 and pT&S knockdown by si-FOXP1 is measured with the EdU incorporation assay. Red fluorescence represents EdU labeled cells. The EdU-positive cells ratio were shown on the right. Data are presented as the mean ± SEM. n = 5-8 for each group. *p < 0.05; **p < 0.01; ***p < 0.001, unpaired Student's t-test.
- (G) Representative GO terms of DEGs in si-NC and si-FOXP1 groups. DEGs were identified by p value and FDR <0.05.
- (H) The expression of senescence marker and the SASP between the si-NC group and si-FOXP1 group.
- (I) ChIP-PCR using the FOXP1 antibody at the CDKN1A promoter.
- (J) SA-β-gal staining in COV434 upon administration of fisetin, quercetin and dasatinib in cells with knockdown of FOXP1. Scale bar, 100 μm.
- (K) The percentage of SA β-gal-positive cells. Data are presented as the mean ± SEM. n = 5-8 for each group.
- (L) Western blotting of protein related to the Nod-like receptor signaling pathway, NF-kappa B signaling pathway, cellular senescence and DNA damage in COV434.
- (M) Proliferation of COV434 upon administration of fisetin, quercetin and dasatinib in cells with knockdown of FOXP1 is measured with the EdU incorporation assay. Red fluorescence represents EdU labeled cells. The EdU-positive cells ratio were shown on the right. Data are presented as the mean ± SEM. n = 5-8 for each group. **p < 0.01; ***p < 0.001, unpaired Student's t-test.

- (B) Immunofluorescence staining for CD31 and α -SMA in young, middle and old human ovarian vessels. Scale bar, 100 μ m.
- (C) UMAP visualization of endothelial cells sub-clusters (left) and smooth muscle cells sub-clusters (right).
- (D) Beeswarm plots showing the specific markers of sub-clusters.
- (E) Left: representative GO terms of different cell types. Right: heatmap showing top 50 marker genes in each cell type.
- (F) Heatmaps showing the upregulated (above, orange) and downregulated (below, blue) DEGs for each sub-cluster between three aged groups (O/Y, M/Y, O/M).
- (G) Representative shared KEGG terms of age-related DEGs in different sub-clusters.
- (H) Violin plot showing the expression of CDKN1A in ECs and SMCs.
- (I) Representative images of anti-CDKN1A in blood vessels by IHC between three groups. Scale bar, 200 μ m.
- Ridge plot showing the shift of SASP gene set score with age in smooth muscle cells (upper) and endothelial cells (lower).

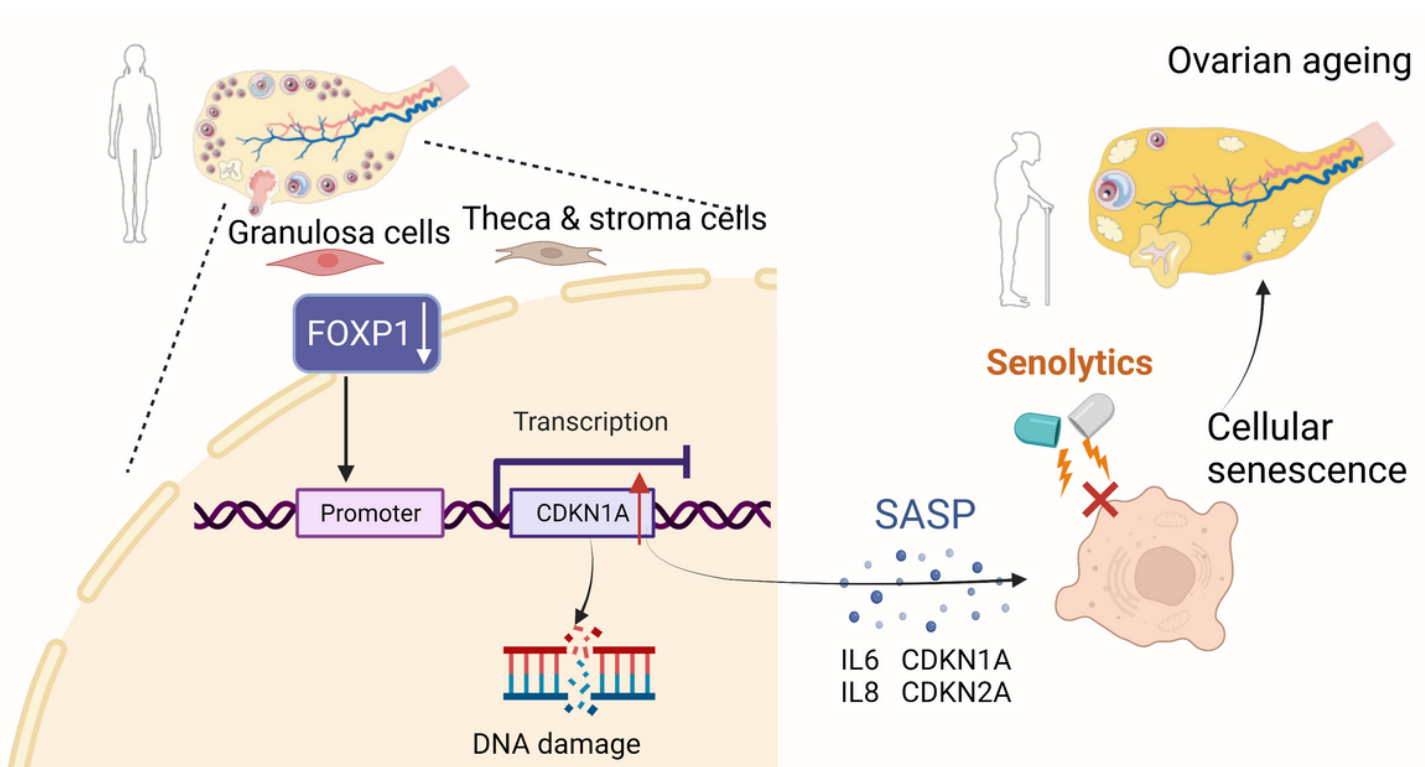


Figure 9

Supplementary Files

This is a list of supplementary files associated with this preprint. Click to download.

- [20220505Supplementary.docx](#)
- [supplementaltables.zip](#)